DEUTSCHES ELEKTRONEN-SYNCHROTRON **DESY**

DESY 89–121
PITHA 89/20
September 1989



# Test of QED by High Energy Electron-Positron Collisions

H.-U. Martyn

*I. Physikalisches Institut, RWTH Aachen*

ISSN 0418-9833

NOTKESTRASSE 85 · 2 HAMBURG 52

To be sure that your preprints are promptly included in the
HIGH ENERGY PHYSICS INDEX ,
send them to the following address ( if possible by air mail ) :

DESY
Bibliothek
Notkestrasse 85
2 Hamburg 52
Germany

DESY 89-121
PITHA 89/20
September 1989

ISSN 0418-9833

# Test of QED by High Energy Electron–Positron Collisions *

Hans – Ulrich Martyn
I. Physikalisches Institut, RWTH Aachen
Sommerfeldstraße, D 5100 Aachen, Germany

August 1989

## Contents



*To appear in 'Quantum Electrodynamics', T. Kinoshita, editor, World Scientific, Signapore

# 1 Introduction

High energy electron–positron collision experiments have provided a large amount of information and contributed considerably to our understanding of particle physics. Despite its high potential to search for new phenomena, one of the main objectives to construct $e^+e^-$ colliders was and still is to test the validity of Quantum Electrodynamics (QED) at large momentum transfers. The particularly clean initial state offers an ideal laboratory to investigate the following basic lowest order processes

- photon pair production
$$e^+e^- \to \gamma\gamma\,, \tag{1}$$
- lepton pair production ($l = e,\ \mu,\ \tau$, or new kind)
$$e^+e^- \to l^+l^-\,, \tag{2}$$
- hadron formation through quark pair production ($q = u,\ d,\ s,\ c,\ b$, or new kind)
$$e^+e^- \to q\bar{q}\,, \tag{3}$$
- fermion pair production through photon–photon scattering $\gamma\gamma \to f\bar{f}$ ($f = l,\ q$) via
$$e^+e^- \to e^+e^- f\bar{f}\,. \tag{4}$$

These processes have been extensively studied at all $e^+e^-$ colliders, covering the large range of centre of mass energy from 1 to 60 GeV, which will very soon be extended to 100 GeV. With the operation of high energy machines, like PETRA, PEP and TRISTAN, it became apparent that it is not sufficient to describe these processes by QED alone. The weak interaction mediated through the intermediate vector boson $Z^0$ and the strong interaction among the final state hadrons become important with increasing centre of mass energy. Gauge theories propose a unified description of electromagnetic and weak interactions, Electroweak Interaction or Quantum Flavourdynamics (QFD), and strong interactions between quarks and gluons, Quantum Chromodynamics (QCD). Various attempts to arrive at a unified theory have been made, the most successful one up to now being the so called Standard Theory based on the $SU(3) \times SU(2) \times U(1)$ symmetry.

QED remains a consistent theory within the embracing standard theory and can be tested by itself provided the following conditions are fullfilled [1]:

1. The characteristic invariants of a process, the centre of mass energy squared $s$ and the space-like momentum transfer squared $Q^2$, have to be small compared to $m_Z^2$, the scale given by the $Z^0$ mass.

2. The experimental precision should be lower than $\mathcal{O}(s/m_Z^2)$ or $\mathcal{O}(Q^2/m_Z^2)$.



Both criteria are not always satisfied in high energy $e^+e^-$ experiments, the momentum transfers reach $s/m_Z^2 \sim 0.35$ while the typical experimental precision is a few percent. Large momentum transfers imply that only special reactions or certain distributions can be used for pure QED tests, where QFD and QCD effects are either neglibible or can be treated as small corrections. With regard to the experimental precision of $e^+e^-$ experiments it is often sufficient to perform QED calculations up to the next to leading order in the fine structure constant $\alpha$, which is $\mathcal{O}(\alpha^3)$ for the two body reactions. These higher orders can be checked explicitly by detecting additional photons in the basic reactions (1) - (4). This has to be compared to low energy high precision measurements like the anomalous magnetic moments of leptons, the Lamb shift and the hyperfine structure splittings (discussed in separate articles of this book), where QED corrections up to the forth and fifth order in $\alpha$ have been calculated. Therefore high energy $e^+e^-$ experiments are complementary by testing QED at very large momentum transfers or equivalently at very small distances.

A major task of QED is concerned with the detailed and precise calculation of higher order radiative effects. Large efforts have been made to implement them into Monte Carlo programs with realistic detector and analysis simulation in order to verify them with experimental data. These tests are of prime importance for the validity of QED and can be considered as a prerequisite to disentangle QFD and QCD effects. They can also be used to search for or set limits on a possible substructrure of the elementary fermions.

The photon pair production $e^+e^- \to \gamma\gamma$, reaction (1), provides a very clean QED test. It proceeds in lowest order $\alpha^2$ via single electron exchange. Also higher order contributions can be entirely described by QED alone, the first order weak corrections being completely negligible.

The $e^+e^-$ annihilation into a fermion pair $e^+e^- \to f\bar{f}$, reactions (2) and (3), belongs to the most simple processes. The production cross section in lowest order receives contributions from photon and $Z^0$ exchange resulting in a sum of pure QED, pure weak and interference terms with a characteristic energy dependence

$$\frac{d\sigma}{d\Omega} = \frac{d\sigma}{d\Omega}^{QED} (\sim \frac{\alpha^2}{s}) + \frac{d\sigma}{d\Omega}^{interference} (\sim \alpha \cdot G) + \frac{d\sigma}{d\Omega}^{weak} (\sim G^2 \cdot s)$$

($G$ = Fermi coupling constant). For quark pair production additional QCD corrections have to be applied. The QED cross section decreases as $1/s$ while the pure weak cross section rises with $s$. At the PETRA, PEP and TRISTAN $e^+e^-$ colliders, even at the highest energies, QED is still the dominating force, the purely weak contributions being only $\sim 2\%$ for lepton pair production but reaching $\sim 50\%$ for quark pair production. However, the electroweak interference between the photon and the $Z^0$ leads to appreciable measurable asymmetries in the fermion angular distributions, which are partly counteracted by practically energy independent higher order QED contributions. At SLC and LEP the fermion pair production will be completely dominated by $Z^0$ formation.

In recent years photon–photon scattering of reaction (4) which proceeds via forth order in $\alpha$ has received special attention. QED tests concentrate on two–photon lepton pair production while hadron final states offer the possibility to study QCD effects and resonance production. The momentum transfers are moderate compared

to the annihilation diagrams, thus providing less stringent QED bounds. However, as an $\mathcal{O}(\alpha^4)$ process it has an interest on its own right.

In this article the phenomenology and experimental results of QED tests in high energy $e^+e^-$ collisions will be presented. Since QED can only be seen in the context of QFD a brief review on electroweak phenomena will be given as well. The material comprises results from the experiments at PETRA, PEP and TRISTAN as published until July 1989.

# 2 Interaction Lagrangians and couplings

The standard theory [2,3,4] combines the electromagnetic, weak and strong interactions between elementary particles into an unified renormalizable theory. It is based on local gauge invariance, which is then spontaneously broken in order to generate the masses of the particles. Although known to be unsatisfactory (e.g. 17 free parameters in the minimal electroweak model) and leaving many questions open, it is still the most successful unified theory and has survived all experimental tests so far. For recent reviews on the status of the electroweak standard model see e.g. [5,1].

The basic theoretical foundations can be found in modern text books. Here only the most important ingredients of the electroweak standard theory relevant for the understanding of $e^+e^-$ reactions will be briefly outlined [6].

## 2.1 The electromagnetic interaction

Quantum Electrodynamics describes the electromagnetic interaction of charged particles with photons. The dimensionless coupling strength is given by the electric charge ($\alpha = e^2/4\pi = 1/137.0359895(61)$ in the low energy Thomson limit). Of special interest is the $ff\gamma$ coupling of a charged fermion (Dirac field $\psi(x)$, charge $e_f = Q_f\, e$) to the photon field $A_\mu(x)$ with the interaction Lagrangian

$$\mathcal{L}_I^{em} = -e_f\, \bar{\psi}(x)\, \gamma_\mu\, \psi(x)\, A^\mu(x)\,. \tag{5}$$

The Lagrangian is invariant under parity and charge conjugation. It is also invariant under a local U(1) gauge transformation which implies a conserved vector current

$$J_\mu^{em}(x) = \bar{\psi}(x)\, \gamma_\mu\, \psi(x) \tag{6}$$

and completely fixes the interaction. The electromagnetic interaction Lagrangian can now being written as

$$\mathcal{L}_I^{em} = -e_f\, J_\mu^{em}(x)\, A^\mu(x)\,. \tag{7}$$

## 2.2 The electroweak interaction

Quantum Flavourdynamics describes the electromagnetic and weak interactions of fermions and bosons with the gauge fields and among the gauge bosons themselves.



It is a renormalizable gauge theory which was first proposed by Glashow [2], Salam [3] and Weinberg [4] for the leptonic sector and has later been extended to the quark sector [7]. The minimal model is based on the group $SU(2) \times U(1)$ with a triplet of gauge fields for the weak isospin group of $SU(2)$ and a singlet gauge field for the weak hypercharge group of $U(1)$. Mass generation of all particles is provided through symmetry breaking by the Higgs mechanism, which introduces an additional scalar Higgs doublet and results in the four physical gauge fields, the massless photon $\gamma$ and the massive intermediate vector bosons $Z^0$, $W^+$ and $W^-$. The symmetry is spontaneously broken from $SU(2) \times U(1)$ to $U(1)_{em}$ of electromagnetism. The coupling constants are related by the unification condition

$$e = g\, \sin\theta_W\,, \tag{8}$$

where $\theta_W$ is called the weak mixing angle. The relation to the charged weak interaction (Fermi coupling constant $G = 1.16637(2)\, 10^{-5}\, GeV^{-2}$ from $\mu$ decay) is given in the tree approximation by

$$\frac{G}{\sqrt{2}} = \frac{g^2}{8\, m_W^2} = \frac{e^2}{8\, \sin^2\theta_W\, m_W^2}\,. \tag{9}$$

Together with

$$m_W = m_Z\, \cos\theta_W \tag{10}$$

the masses of the intermediate bosons $m_W$ and $m_Z$ are determined by a measurement of $\alpha$, $G$ and $\sin^2\theta_W$.

In the standard theory all fermions are represented as left-handed doublets and right-handed singlets of weak isospin $I^f$. However, there exist no right-handed neutrinos, i.e. neutrinos are massless. There are three generations of leptons, $(\nu_e, e^-)$, $(\nu_\mu, \mu^-)$ and $(\nu_\tau, \tau^-)$, and three generations of quarks, $(u, d')$, $(c, s')$ and $(t, b')$, where the top quark $t$ still awaits its experimental discovery. The quarks $q'$ represent the weak eigenstates. Transitions between lepton families are not allowed, while the quark generations are mixed through the weak charged current.

The interaction $ffZ$ between a fermion and the $Z^0$ gauge field $Z_\mu(x)$ can be written analogous to eq. (7) as the weak neutral current interaction Lagrangian

$$\mathcal{L}_I^Z = -\frac{g}{2\, \cos\theta_W}\, J_\mu^Z(x)\, Z^\mu(x) \tag{11}$$

with the weak neutral current

$$J_\mu^Z(x) = \bar{\psi}(x)\, \gamma_\mu\, (g_V^f - g_A^f\, \gamma^5)\, \psi(x)\,. \tag{12}$$

This Lagrangian violates parity and charge conjugation. The vector and axial vector couplings are defined as

$$g_V^f = I_3^f - 2\, Q_f\, \sin^2\theta_W\,, \tag{13}$$

$$g_A^f = I_3^f\,, \tag{14}$$

Table 1: Quantum numbers and coupling constants of the elementary fermions to the electroweak neutral current. Numerical values are given for $\sin^2\theta_W = 0.23$

| Fermion | $Q_f$ | $I_3^f$ | $g_V^f$ | | $g_A^f$ |
|---|---|---|---|---|---|
| $\nu_e$, $\nu_\mu$, $\nu_\tau$ | 0 | $+\frac{1}{2}$ | $+\frac{1}{2}$ | $+0.50$ | $+0.50$ |
| $e^-$, $\mu^-$, $\tau^-$ | $-1$ | $-\frac{1}{2}$ | $-\frac{1}{2}+2\sin^2\theta_W$ | $-0.04$ | $-0.50$ |
| $u$, $c$, $t$ | $+\frac{2}{3}$ | $+\frac{1}{2}$ | $+\frac{1}{2}-\frac{4}{3}\sin^2\theta_W$ | $+0.19$ | $+0.50$ |
| $d$, $s$, $b$ | $-\frac{1}{3}$ | $-\frac{1}{2}$ | $-\frac{1}{2}+\frac{2}{3}\sin^2\theta_W$ | $-0.35$ | $-0.50$ |

where $I_3^f$ is the third component of the weak isospin. The experimentally determined value of the weak mixing angle using all available information (assuming a top quark mass of $m_t = 45\,GeV$ and a Higgs mass of $m_H = 100\,GeV$) is [8]

$$\sin^2\theta_W = 0.230 \pm 0.0048\ .$$

The quantum numbers and coupling constants of the fermions are summarized in Table 1.

The complete electroweak neutral current interaction Lagrangian then becomes

$$\mathcal{L}_I^{NC} = \mathcal{L}_I^{em} + \mathcal{L}_I^{Z}\ . \tag{15}$$

# 3 Cross sections in lowest order

At the energies discussed in this article electrons and positrons couple to the neutral gauge bosons ($e^+e^-\gamma$, $e^+e^-Z$). Couplings to the Higgs boson are suppressed by $m_e/m_W$ factors and can be safely neglected. In this section cross section formulas for the standard reactions will be given in lowest order in the general frame of QFD, and also for the embedded special case of QED. Only unpolarized electron and positron beams will be considered, since so far experiments with transverse polarized beams did not surpass an exploratory study. This situation may change at the next generation of $e^+e^-$ colliders, SLC and LEP, where experiments hope to profit from longitudinal polarization. Higher order radiative corrections will be treated in detail in section 4.

## 3.1 $e^+e^- \to \gamma\gamma$

Two photon production $e^+e^- \to \gamma\gamma$ is a pure QED process mediated by the two diagrams of $t$ and $u$ channel electron exchange of Fig. 1. Defining $\theta$ as the polar angle between the electron and photon the differential cross section for $e^+e^- \to \gamma\gamma$ in second order QED is

$$\frac{d\sigma}{d\Omega} = \frac{\alpha^2}{s}\frac{1+\cos^2\theta}{\sin^2\theta}\ . \tag{16}$$



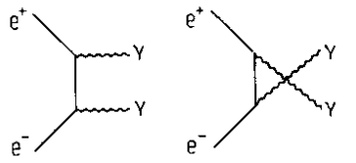


Figure 1: Lowest order diagrams for $e^+e^- \to \gamma\gamma$

Typically for $t$ channel exchange the cross section is steeply rising in the forward and backward region and appears to be singular as $\theta$ approaches 0 or $\pi$. This is due to the fact that the electron mass has been neglected. The denominator $\sin^2\theta$ should be replaced by $1-\beta_e^2\cos^2\theta \simeq \sin^2\theta + 4\,m_e^2/s$, where $\beta_e = p_e/E_e = \sqrt{1-4\,m_e^2/s}$ is the velocity of the electron. The correction term $4\,m_e^2/s$ reaches the level $10^{-3}$ only in the direction very close to the beams if $\theta$ or $\pi-\theta \le 30/\sqrt{s}\ [GeV]\ mrad$. For detectors with limited acceptance $\theta > \theta_{min}$ the integrated total cross section becomes

$$\begin{aligned}\sigma(e^+e^- \to \gamma\gamma) &= \int_{\theta_{min}}^{\pi/2}\frac{d\sigma}{d\Omega}d\Omega \\ &= \frac{2\,\pi\,\alpha^2}{s}\left\{\ln\frac{1+\cos\theta_{min}}{1-\cos\theta_{min}} - \cos\theta_{min}\right\}\ .\end{aligned} \tag{17}$$

The integration is performed over one hemisphere to take into account that both photons are indistinguishable. Apart from QED radiative corrections this reaction should also at very high energies be completely described by electron exchange.

## 3.2 $e^+e^- \to f\bar{f}$

The $e^+e^-$ annihilation into a fermion pair $e^+e^- \to f\bar{f}$ with $f$ being a $\mu$, $\tau$ or quark proceeds in lowest order via photon and $Z^0$ exchange as sketched in Fig. 2 (for $f = e$ additional $t$ channel diagrams have to be added, see below). Defining $\theta$ as the polar angle between the incoming electron and the outgoing fermion the electroweak differential cross section for $e^+e^- \to f\bar{f}$ including mass effects is given in lowest order by

$$\begin{aligned}\frac{d\sigma}{d\Omega} &= \frac{\alpha^2}{4\,s}N_f^c\,\beta_f\left\{C_1(1+\cos^2\theta) + \beta_f\,C_2\cos\theta + (1-\beta_f^2)\,C_3\,\sin^2\theta\right\}\ , \\ C_1 &= Q_f^2 - 2\,g_V^e\,g_V^f\,Q_f\,\Re(\chi) + (g_V^{e\,2}+g_A^{e\,2})(g_V^{f\,2}+g_A^{f\,2})\,|\chi|^2\ , \\ C_2 &= \quad -4\,g_A^e\,g_A^f\,Q_f\,\Re(\chi) + 8\,g_V^e\,g_V^f\,g_A^e\,g_A^f\,|\chi|^2\ , \\ C_3 &= Q_f^2 - 2\,g_V^e\,g_V^f\,Q_f\,\Re(\chi) + (g_V^{e\,2}+g_A^{e\,2})\,g_V^{f\,2}\,|\chi|^2\ .\end{aligned} \tag{18}$$

Here $N_f^c$ is a colour factor (1 for leptons and 3 for quarks), $\beta_f = p_f/E_f = \sqrt{1-4\,m_f^2/s}$ is the velocity of the fermion and $g_V^e$, $g_V^f$, $g_A^e$, $g_A^f$ are the vector and axial vector couplings of the electron and fermion given in Table 1.

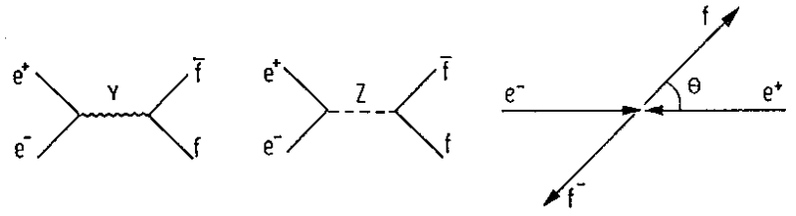


Figure 2: Lowest order diagrams for $e^+e^- \to f\bar{f}$ and definition of the polar angle $\theta$

The function $\chi$ is given by the coupling strengths and the $Z^0$ propagator and depends on the renormalization scheme. Choosing $\alpha$, $m_Z$ and $\sin^2\theta_W$ (on-shell scheme) one has

$$\chi_I = \frac{1}{4\sin^2\theta_W\cos^2\theta_W}\,\frac{s}{s-m_Z^2+im_Z\Gamma_Z}\,. \tag{19}$$

In this scheme the measured cross sections can be directly compared to the lowest order Born term calculations, once 'reduced QED' radiative corrections are applied to the data (see section 4). The disadvantage of this parametrization is that it needs the weak mixing angle and the $Z^0$ mass as input, where the latter has still large experimental errors. Alternatively one can use the parameters $\alpha$, $G$ and $m_Z$ ($Z$-mass scheme) and obtains

$$\chi_{II} = \frac{G(1-\Delta r)\,m_Z^2}{2\sqrt{2}\,\pi\,\alpha}\,\frac{s}{s-m_Z^2+im_Z\Gamma_Z}\,. \tag{20}$$

The factor $(1-\Delta r)$ accounts for the radiative corrections of the Fermi coupling constant derived from $\mu$ decay. It is predicted to be $\Delta r = 0.0713 \pm 0.0013$ [5] (assuming a top quark mass $m_t = 45\,GeV$ and a Higgs mass $m_H = 100\,GeV$). In this scheme only well known quantities enter and the dependence on the $Z^0$ mass is weak in the interference region. However, the data have to be corrected for the complete electroweak radiative corrections (see section 4).

In many cases it is sufficient to consider the relativistic limit $\beta_f \to 1$, thus

$$\frac{d\sigma}{d\Omega} = \frac{\alpha^2}{4s}\,N_f^c\left\{C_1(1+\cos^2\theta) + C_2\cos\theta\right\}\,. \tag{21}$$

In QED the lowest order differential cross section for $e^+e^- \to f\bar{f}$ via single photon exchange simplifies to

$$\frac{d\sigma}{d\Omega} = \frac{\alpha^2}{4s}\,N_f^c\,Q_f^2\,\left\{1+\cos^2\theta\right\}\,, \tag{22}$$

and the total cross section becomes

$$\sigma(e^+e^- \to f\bar{f}) = \frac{4\pi\alpha^2}{3s}\,N_f^c\,Q_f^2 = \sigma^0\,N_f^c\,Q_f^2\,. \tag{23}$$



The quantity

$$\sigma^0 = \frac{4\pi\alpha^2}{3s} = \frac{86.8\,nb}{s\,[GeV^2]}\,. \tag{24}$$

is called the pointlike QED cross section for asymptotic lepton pair production and is often used to present normalized total cross section data as

$$R_{f\bar{f}} = \frac{\sigma(e^+e^- \to f\bar{f})}{\sigma^0} = N_f^c \cdot C_1\,. \tag{25}$$

The QFD differential cross section eq. (21) has a term symmetric in $\cos\theta$ and another term linear in $\cos\theta$. The symmetric part is a sum of purely electromagnetic, interference and purely weak contributions, while the asymmetric part contains only interference and purely weak terms. Note that the asymmetry is not a parity violating effect but solely due to the interference of the vector and axial vector currents. Parity violation can only be observed by using longitudinally polarized $e^\pm$ beams or by analyzing the final state fermion polarization.

In the total cross section the term linear in $\cos\theta$ drops out and the rate is proportional to the coefficient $C_1$ of eq. (18), which is sensitive to the vector couplings in the interference region. Since the weak mixing angle $\sin^2\theta_W$ is close to $1/4$ and therefore the electron vector coupling is close to zero, the weak contributions are still small up to centre of mass energies around $\sqrt{s} \le m_Z/2$. This means that total cross section measurements could serve as a test of QED for not too high energies. The behaviour of $R_{f\bar{f}}$, the total cross section of fermion pair production normalized to the pointlike QED cross section, as a function of the centre of mass energy is displayed in Fig. 3 for $\mu$ (or $\tau$) pair production and hadron production $e^+e^- \to \sum q\bar{q} \to hadrons$. $R_{\mu\mu}$ is very close to one up to energies around $\sqrt{s} = 55\,GeV$ and then begins to rise towards a value of $\sim 200$ at the $Z^0$ resonance. For hadron production one notices the charm and bottom thresholds (araound 4 and 10 $GeV$) and a subsequently fairly constant level. Beyond $\sqrt{s} = 35\,GeV$ $R_{had}$ starts to increase, by about 50% at 60 $GeV$ and reaching finally values of $\sim 4000$ at the $Z^0$ pole.

On the other hand the differential cross section exhibits a sizeable asymmetry at PETRA, PEP and TRISTAN energies. A convenient quantity is the forward backward charge asymmetry defined as

$$\begin{aligned} A_{f\bar{f}} &= \frac{N_F - N_B}{N_F + N_B}\,, \\ &= \frac{3}{8}\frac{C_2}{C_1}\,, \\ &\simeq -\frac{3}{2}\,\frac{g_A^e\,g_A^f}{Q_f}\,\Re(\chi)\,. \end{aligned} \tag{26}$$

Here $N_F$ is the number of fermions produced in the forward direction ($\cos\theta \ge 0$) and $N_B$ is the number of fermions produced in the backward direction ($\cos\theta \le 0$). The approximation holds for the interference region where $s \ll m_Z^2$ and indicates that the asymmetries are larger by a factor $1/Q_f$ for quarks than for leptons. The expected fermion asymmetries $A_{f\bar{f}}$ as a function of the centre of mass energy are shown in Fig.

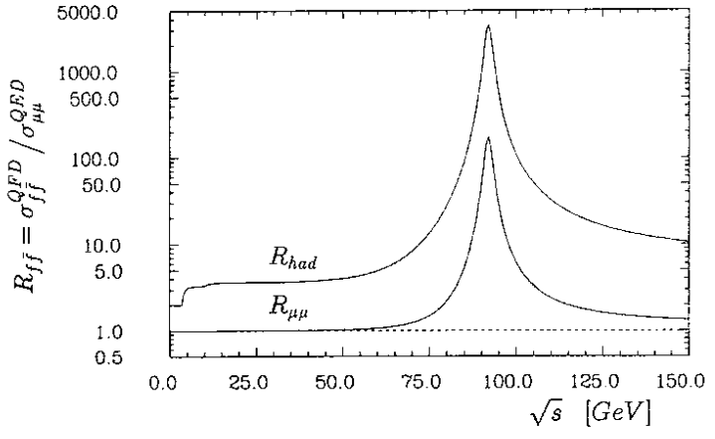


Figure 3: Normalized total cross sections $R_{f\bar{f}}$ as a function of the centre of mass energy $\sqrt{s}$. The curves show $R_{\mu\mu}(e^+e^- \to \mu^+\mu^-)$ and $R_{had}(e^+e^- \to \sum q\bar{q} \to hadrons)$ for 5 quarks

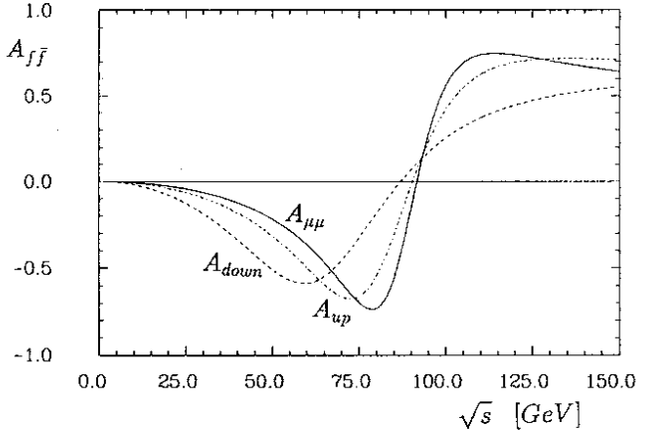


Figure 4: Forward backward charge asymmetries $A_{f\bar{f}}$ as a function of the centre of mass energy $\sqrt{s}$ for $e^+e^- \to f\bar{f}$. The curves show $A_{\mu\mu}$ for $\mu$ or $\tau$ pair production, $A_{up}$ for *up* type quarks and $A_{down}$ for *down* type quarks



4. They are negative below the $Z^0$ resonance and after passing through a maximimum they change their sign at energies close to the $Z^0$ mass. The shape of the differential cross section essentially determines the axial vector couplings and cannot be used for QED tests.

### 3.3 $e^+e^- \to e^+e^-$

In Bhabha scattering $e^+e^- \to e^+e^-$ there are in addition to the annihilation graphs two space-like diagrams for $t$ channel exchange (Fig. 5). Defining $\theta$ as the polar angle between the incoming and outgoing electron the differential cross section for $e^+e^- \to e^+e^-$ in second electroweak order was calculated in ref. [9]

$$\begin{aligned}
\frac{d\sigma}{d\Omega} &= \frac{\alpha^2}{8\,s}\left\{4\,B_1 + B_2\,(1-\cos\theta)^2 + B_3\,(1+\cos\theta)^2\right\}\,, \qquad (27)\\
B_1 &= \left(\frac{s}{t}\right)^2 \left|1 + (g_V{}^2 - g_A{}^2)\,\chi(t)\right|^2\,,\\
B_2 &= \left|1 + (g_V{}^2 - g_A{}^2)\,\chi(s)\right|^2\,,\\
B_3 &= \frac{1}{2}\left|1 + \frac{s}{t} + (g_V + g_A)^2\,(\frac{s}{t}\,\chi(t) + \chi(s))\right|^2\\
&\quad + \frac{1}{2}\left|1 + \frac{s}{t} + (g_V - g_A)^2\,(\frac{s}{t}\,\chi(t) + \chi(s))\right|^2\,.
\end{aligned}$$

Here $t = -s/2\,(1-\cos\theta)$ is the space-like momentum transfer squared, the function $\chi(s)$ is one of equations (19) or (20) and $\chi(t)$ is the same function with $s$ replaced by $t$, $g_V$ and $g_A$ denote the vector and axial vector couplings of the electron as given in Table 1.

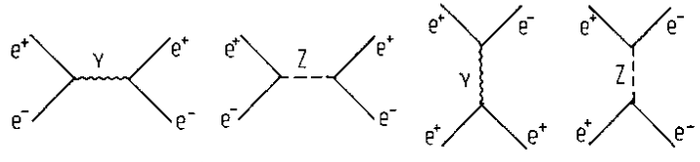


Figure 5: Lowest order diagrams for $e^+e^- \to e^+e^-$

The differential cross section for Bhabha scattering in second order QED via photon exchange is

$$\frac{d\sigma}{d\Omega} = \frac{\alpha^2}{4\,s}\,\frac{(3+\cos^2\theta)^2}{(1-\cos\theta)^2}\,. \qquad (28)$$

The differential cross section is dominated by large $t$ channel contributions and shows therefore a strong forward peaking (the total cross section is infinite because of

the long range force due to photon exchange). Bhabha scattering is thus extremely useful to determine with high rates the luminosity in $e^+e^-$ experiments at very small angles ($\theta \simeq 30 mrad$), where electroweak effects can be completely neglected as the propagator term $\chi(t) \to 0$ for $t \to 0$.

In the central and backward region the differential cross section is sensitive to electroweak interference. However, due to cancelations of $s$ and $t$ diagrams and due to the fact that the electron vector coupling is close to zero, the expected effects are rather small. As an example Fig. 6 shows the ratio of the electroweak to the QED cross section at a typical PETRA centre of mass energy $\sqrt{s} = 35\,GeV$. The maximum deviation is about $-2.5\%$ in the backward hemisphere, close to the achieved experimental resolution. This means that after applying the small corrections due to the standard model Bhabha scattering could be used for QED tests.

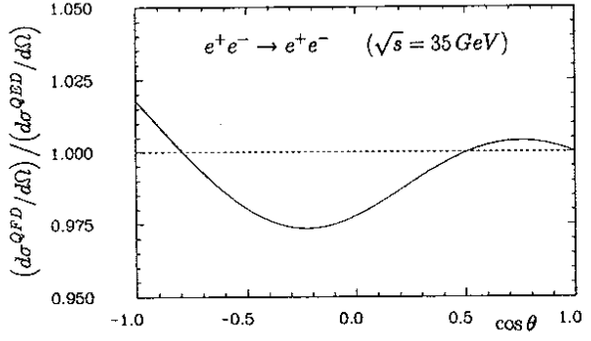


Figure 6: The electroweak differential Bhabha cross section divided by the QED cross section at $\sqrt{s} = 35\,GeV$

# 4 Radiative corrections

The second order $e^+e^-$ two body reactions described in section 3 represent an ideal situation. Any real experiment has to deal with higher order processes involving either more than two particles in the final state or virtual effects (loop diagrams). Examples of the first type are photon bremsstrahlung off fermions with a probability increasing with decreasing mass, leading e.g. to the final states

$$e^+e^- \to \gamma\gamma\gamma,\ \gamma\gamma\gamma\gamma,\ \ldots$$
$$e^+e^- \to f\bar{f}\gamma,\ f\bar{f}\gamma\gamma,\ \ldots$$

Examples of the second type are loop corrections appearing in boson or fermion propagators, vertices and box diagrams. The size of these so called radiative corrections depends on the actual experimental set up and event selection criteria.



Both QED and weak contributions modify the measured cross section which can formally be written as

$$\frac{d\sigma}{d\Omega}^{meas} = \frac{d\sigma}{d\Omega}^{0} \left(1 + \delta^{QED} + \delta^{weak}\right), \qquad (29)$$

where $d\sigma^0/d\Omega$ is the Born cross section. The radiative corrections are calculable order by order. Complete calculations for the $e^+e^-$ processes (1), (2) and (3) have been performed up to $\mathcal{O}(\alpha^3)$, which means first order corrections to the lowest order cross sections. In some special cases $\mathcal{O}(\alpha^4)$ cross sections have been computed.

Let us consider the first order corrections. The radiative corrections can be divided in two parts: virtual corrections to the non radiative lowest order diagrams and photon bremsstrahlung.

The virtual corrections are obtained by adding loops to the internal lines, known as vacuum polarization, and by adding an internal photon line in all possible ways to the external lines, known as vertex corrections and box diagrams. These diagrams are of $\mathcal{O}(\alpha^4)$, their interference with the lowest order diagrams leads to $\mathcal{O}(\alpha^3)$ cross sections.

The bremsstrahlung diagrams are obtained by adding an external photon line to the lowest order diagrams, thus giving $\mathcal{O}(\alpha^3)$ contributions.

Corrections involving photons and massive gauge bosons have to be treated differently. Virtual QED corrections $\delta_v^{QED}$ exhibit infrared divergences caused by the photon propagator $1/k$ in the soft photon limit $k \to 0$. They can be regularized by introducing a fictitious photon mass $\lambda$, which is of course unphysical but drops out after summing up all divergences. Similarly, divergences arise for the bremsstrahlung, where an infinite number of photons are emitted as $k \to 0$, and in collinear configurations where a photon is emitted along the direction of one of the initial or final state particles. In most cases the experiments do not detect radiated photons, one reason being the limited solid angular acceptance in particular along the beam directions. But even if they had photon detection capabilities the finite experimental resolution $\Delta E$ does not allow to distinguish between single and multiple photon emission if $k < \Delta E$. The bremsstrahlung calculations are therefore split in an infrared divergent soft photon part $\delta_s^{QED}$ and a finite hard photon part $\delta_h^{QED}$. The renormalizability of QED assures that each order of the perturbation expansion is calculable and finite. The divergences from the virtual corrections exactly cancel the divergences from the soft photon bremsstrahlung, such that the final QED correction

$$\delta^{QED} = \delta_v^{QED} + \delta_s^{QED} + \delta_h^{QED}$$

remains finite.

The evaluation of the weak radiative corrections is much more elaborate. Although numerous calculations exist they are sometimes difficult to compare since no common choice of basic parameters and/or renormalization scheme has been adopted by the various authors. However, there seems to be agreement that the weak corrections are small compared to the QED corrections (at least at energies below the $Z^0$ pole) when using the physical $Z^0$ mass and the coupling constants renormalized at the mass of the $Z^0$.

Therefore it seems appropriate to separate the radiative correction calculations at the one-loop level into three categories with the following definitions of the notion:

1. Electromagnetic corrections to the $\gamma$ or electron exchange diagrams consisting of virtual photon and bremsstrahlung contributions and the fermionic vacuum polarization of the photon. They are called 'reduced QED corrections' and are model independent but depend on the experimental conditions.

2. Electromagnetic corrections to the $Z^0$ exchange diagrams consisting of virtual and bremsstrahlung contributions in all possible combinations. They are dependent on the model parameters as well as on the experimental cuts. Together with the above corrections they are called 'full QED corrections'.

3. Weak (non-photonic) corrections to both $\gamma$ and $Z^0$ exchange diagrams. They contain dynamical aspects of the electroweak model and depend sensitively on the renormalization scheme.

A convenient way to compare measurements with the lowest order theory is to unfold the data by using the calculated radiative corrections, thus arriving at 'lowest order data'. This method to present results was applied by almost all the experiments at PETRA, PEP and TRISTAN. At these energies the most important contributions come from QED effects and the electroweak radiative corrections play a minor rôle. This situation may be different at SLC and LEP, where the 'lowest order data' depend on the electroweak theory which one wants to test in detail. Here it may be more sensible to compare the acceptance corrected data with the specific electroweak model. However, in both cases it is very important to have event generators including higher order radiative corrections in the form of Monte Carlo programs which allow to simulate the experimental conditions as precisely as possible.

In the following the QED and weak radiative corrections will be discussed separately for the basic two body reactions. A detailed discussion of radiative corrections in $e^+e^-$ lepton pair production including cross section formulas can be found in [10].

## 4.1 $e^+e^- \to \gamma\gamma,\ \gamma\gamma\gamma$

The complete set of diagrams leading to $\mathcal{O}(\alpha^3)$ cross sections for $e^+e^- \to \gamma\gamma,\ \gamma\gamma\gamma$ is shown in Fig. 7. Besides the lowest order graphs (a) they consist of virtual corrections to the vertices (b), to the electron propagator (c), box diagrams (d) and photon bremsstrahlung (e).

The differential cross section formulas are rather involved and can be found, e.g., in ref. [10]. The total $\mathcal{O}(\alpha^3)$ cross section is

$$\begin{aligned}\sigma(e^+e^- \to \gamma\gamma, \gamma\gamma\gamma) &= \sigma^{2\gamma} + \sigma^{3\gamma} \qquad (30)\\ &= \sigma^0 \left\{ 1 + \frac{\alpha}{\pi} \frac{1}{2v-1} \left( \frac{4}{3} v^3 - v^2 + \left( \frac{2\pi^2}{3} - 2 \right) v + 2 - \frac{\pi^2}{12} \right) \right\}.\end{aligned}$$

$\sigma^0 = 2\pi\alpha^2(2v-1)/s$ is the lowest order cross section given in section 3.1 and $v = 1/2 \ln(s/m_e^2)$. The correction to $\sigma^0$ increases with energy and amounts to appreciable values of 18.8% and 20.6% at $\sqrt{s} = 30$ and 50 $GeV$.



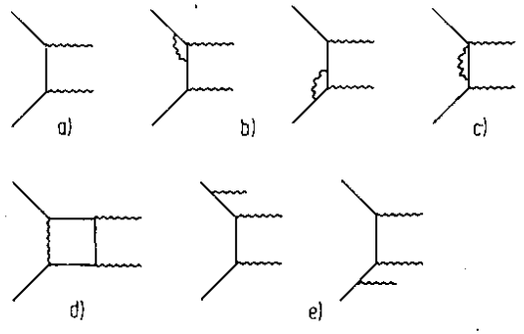


Figure 7: Diagrams leading to $\mathcal{O}(\alpha^3)$ cross section for the reaction $e^+e^- \to \gamma\gamma$. a) Lowest order, b) vertex corrections, c) electron propagator corrections, d) box diagram, e) photon bremsstrahlung. The diagrams with the two external photons interchanged have to be added

The first order weak corrections turn out to be very small, below 1%. Therefore the reaction $e^+e^- \to \gamma\gamma$ can be considered for all practical purposes as a pure QED process even at $Z^0$ energies.

## 4.2 $e^+e^- \to f\bar{f},\ f\bar{f}\gamma$

The lowest order radiative corrections to the reaction $e^+e^- \to f\bar{f}$ are conveniently split into QED corrections and weak corrections. The first order QED correction diagrams to $\gamma$ and $Z^0$ exchange are shown in Figs. 8 and 9. Some first order electroweak correction diagrams are shown in Fig. 10.

The first order QED correction diagrams to $\gamma$ exchange (Fig. 8) consist of the vacuum polarization of the photon (b), vertex corrections (c), box diagrams (d) and photon bremsstrahlung (e). The largest effect of the virtual QED corrections comes from the vacuum polarization of the photon. The electric charge polarizes the surrounding vacuum into fermion antifermion pairs and is thus screened to a lesser degree the closer the distance or the higher the momentum transfer of the scattering particles. This leads to a modification of the photon propagator which can be absorbed in the definition of the now running electromagnetic coupling constant $\alpha$ at momentum transfer $Q^2$

$$\alpha^{-1}(Q^2) = \alpha^{-1} \left\{ 1 - \frac{\alpha}{3\pi} N_f^c \sum_f Q_f^2 \ln \frac{Q^2}{m_f^2} \right\}. \qquad (31)$$

Here $\alpha$ is the fine structure constant obtained from low energy measurements ($Q^2 \sim m_e^2$) and the sum extends over all fermions (leptons and quarks) with $m_f^2 < Q^2$. Inserting the known lepton masses and effective quark masses, e.g. 0.1 $GeV$ for the

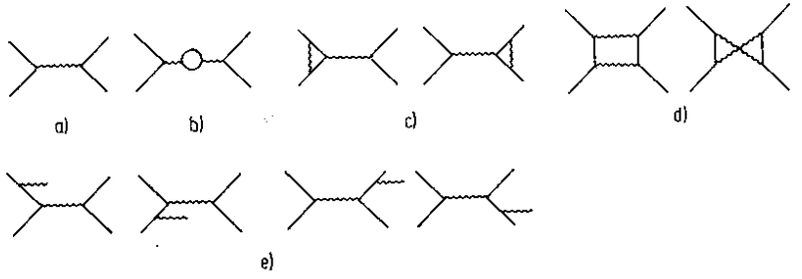


Figure 8: First order QED diagrams to $\gamma$ exchange leading to $\mathcal{O}(\alpha^3)$ cross section for the reaction $e^+e^- \to f\bar{f}$. a) Lowest order, b) photon vacuum polarization, c) vertex corrections, d) box diagrams, e) bremsstrahlung diagrams

light quarks $u$, $d$, $s$, one obtains for a typical PETRA energy of $35\,GeV$ an increased effective coupling constant $\alpha \sim 1/129$ compared to the low energy value of $\sim 1/137$. The above formula is valid for the continuum region away from the vector meson resonances $\rho$, $\phi$, $J/\psi$, $\Upsilon$, etc. A more careful analysis using dispersion relations together with measured cross section data from $e^+e^- \to$ *hadrons* leads to consistent results. The vertex corrections, box diagrams and bremsstrahlung diagrams involve an additional photon with the quantum numbers $J^{PC} = 1^{--}$. The parity of these diagrams is therefore opposite to the parity of the Born graph and their interference induces a forward backward charge asymmetry. As mentioned above the vertex corrections, box diagrams and soft photon bremsstrahlung terms are each divergent by themselves, but the total corrections are finite after summing up all diagrams. Expressions for the individual contributions are rather involved and can be found in [10] and references therein.

For the hard photon bremsstrahlung the largest effect is the radiation off the initial state electrons and positrons. Emission of a photon with energy $k$ leads to a reduced centre of mass energy $s' = 4\,E\,(E-k)$ and thus the rate increases due to the $1/s$ dependence of the cross section. The bremsstrahlung spectrum can be given separately for the initial electron and the final fermion

$$\frac{d\sigma^e}{dk} = \sigma^0(s')\,N_f^c\,\frac{\alpha}{\pi}\left(\ln\frac{s}{m_e^2}-1\right)\left(1+\left(\frac{s'}{s}\right)^2\right)\frac{1}{k}\,, \tag{32}$$

$$\frac{d\sigma^f}{dk} = \sigma^0(s)\,N_f^c\,Q_f^2\,\frac{\alpha}{\pi}\left(\ln\frac{s}{m_f^2}-1+\ln\frac{s'}{s}\right)\left(1+\left(\frac{s'}{s}\right)^2\right)\frac{1}{k}\,. \tag{33}$$

$\sigma^0(s) = 4\,\pi\,\alpha^2/3\,s$ is the lowest order QED total cross section given in section 3.2, and $\sigma^0(s')$ is the total cross section at a reduced centre of mass energy $s'$. Integrating over the photon spectrum for $k > k_0$ gives

$$\sigma^e = \sigma^0\,N_f^c\,\frac{2\,\alpha}{\pi}\left(\ln\frac{s}{m_e^2}-1\right)\left(\ln\frac{E}{k_0}+\frac{1}{2}\ln\frac{s}{m_f^2}-\frac{4}{3}\right)\,, \tag{34}$$



$$\sigma^f = \sigma^0\,N_f^c\,Q_f^2\,\frac{2\,\alpha}{\pi}\left\{\left(\ln\frac{s}{m_f^2}-1\right)\left(\ln\frac{E}{k_0}-\frac{3}{4}\right)+\frac{5}{8}-\frac{\pi^2}{6}\right\}\,. \tag{35}$$

These expressions diverge for $k_0 \to 0$, but the whole cross section remains finite after adding the soft photon part and the virtual corrections.

The total cross section for the QED corrections to the photon exchange diagrams alone takes the form

$$\begin{aligned}\sigma(e^+e^- \to f\bar{f},\,f\bar{f}\gamma) &= \sigma^{ff} + \sigma^{ff\gamma}\,,\\ &= \sigma^0\,(1+\delta_e+\delta_f+\delta_{vp})\,, \qquad (36)\\ \delta_e &= \frac{2\,\alpha}{\pi}\left\{\frac{1}{2}\ln\frac{s}{m_e^2}\ln\frac{s}{m_f^2}-\frac{7}{12}\ln\frac{s}{m_e^2}-\frac{1}{2}\ln\frac{s}{m_f^2}+\frac{\pi^2}{6}+\frac{1}{3}\right\}\,,\\ \delta_f &= \frac{3\,\alpha}{4\,\pi}\,,\\ \delta_{vp} &= \sum_i \frac{2\,\alpha}{\pi}\left\{-\frac{5}{9}+\frac{1}{3}\ln\frac{s}{m_i^2}\right\}\,.\end{aligned}$$

$\delta_e$ contains the virtual, soft and hard bremsstrahlung corrections, while $\delta_f$ is a similar term for the final fermion, and $\delta_{vp}$ is the vacuum polarization of the photon, where the sum runs over the three leptons and six quark flavours (suitable quark masses are $m_u = m_d = 0.032\,GeV$, $m_s = 0.15\,GeV$, $m_c = 1.5\,GeV$, $m_b = 4.5\,GeV$, $m_t = 30\,GeV$).

The corrections discussed so far are called the 'reduced QED corrections' and constitute the major part of the radiative corrections below the $Z^0$ resonance. It is obvious that the electron contribution is by far the most important one. Due to the double log term $\ln(s/m_e^2)\,\ln(s/m_f^2)$ the radiative corrections become large if hard photon emission along the $e^\pm$ beams cannot be rejected experimentally. To illustrate the effect, take as example the reaction $e^+e^- \to \mu^+\mu^-$ at $\sqrt{s} = 35\,GeV$. The $\delta_e$ term contributes a 53% correction, while the vacuum polarization is about 12% and the muonic contribution is entirely negligible. The complete corrections to the total cross sections appear to be extremely large. In practice, however, experimental conditions restrict the acceptable phase space and the corrections become less dramatic.

In order to control the hard photon radiation and the available phase space, experimental cuts on the energy $E_f$ of the final state fermion and the acollinearity angle $\xi$ between the fermion momenta $\vec{p}_f$ are applied, where $\xi = \arccos(-\vec{p}_f \cdot \vec{p}_f)$. To illustrate the effect of radiative corrections for the reaction $e^+e^- \to \mu^+\mu^-$ at $\sqrt{s} = 35\,GeV$, standard experimental conditions of $\xi < 10^0$ and $E_\mu > \sqrt{s}/4$ lead to a total correction of about 25%. The interference of the Born amplitude with the box diagrams and soft photon radiation results in a positive forward backward charge asymmetry, while the hard photons produce a negative asymmetry. The net effect on the observable asymmetry within the polar angle acceptance of $|\cos\theta_\mu| < 0.80$ is a positive correction term of about $+(1.5-2.0)\%$ from QED $\mathcal{O}(\alpha^3)$ radiative corrections.

The diagrams of first order QED corrections to the $Z^0$ exchange graphs are shown in Fig. 9. They contain vertex corrections (b), box diagrams involving $\gamma$ and $Z^0$ lines

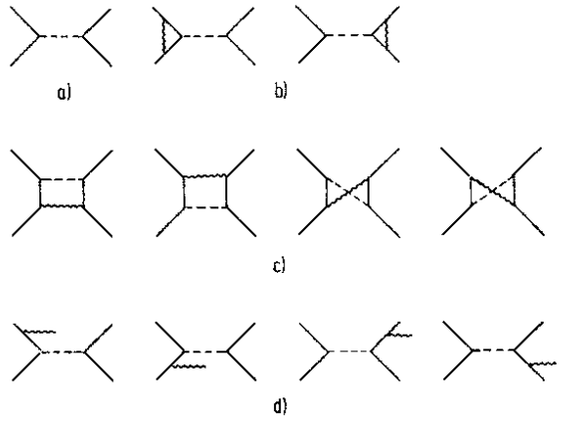


Figure 9: First order QED diagrams to $Z^0$ exchange leading to $\mathcal{O}(\alpha^3)$ cross section for the reaction $e^+e^- \to f\bar{f}$. a) Lowest order, b) vertex corrections, c) box diagrams, d) bremsstrahlung diagrams

(c) and photon bremsstrahlung to the $Z^0$ Born graph (d). Again there appear infrared divergences in the vertex corrections and box diagrams which cancel against those of the soft photon bremsstrahlung. Hard photon initial state radiation further reduces the observable electroweak charge asymmetry in absolute magnitude as it shifts the available centre of mass energy towards lower values away from the $Z^0$ resonance. The size of the effect depends on the experimental selection criteria. Taking all QED corrections to the $\gamma$ and $Z^0$ exchange diagrams as depicted in Figs. 8 and 9 one arrives at the so called 'full QED corrections'.

In order to complete the radiative corrections the purely weak terms have to be included, some of the virtual weak loop diagrams are shown in Fig. 10. Among those the most important one is the self energy diagram to the $Z^0$ (a). Since the standard theory is renormalizable the higher orders are calculable. Due to the finite mass of the weak bosons they are infrared finite. Although a large number of calculations have been performed, the results are difficult to compare since the authors prefer different choices of the input parameters and of the renormalization schemes. This does not apply to QED where the on-shell scheme with $\alpha$ and the fermion masses as parameters has been commonly accepted. For the weak corrections two popular schemes are the on-shell scheme using renormalized parameters $\alpha$, $m_Z$ and $\sin^2\theta_W$ (or equivalently $m_W$ via the relation $\sin^2\theta_W = 1 - m_W^2/m_Z^2$) and the $Z$-mass scheme using $\alpha$, $G$ and $m_Z$. In addition some assumptions on the masses of the yet undiscovered top quark and Higgs (in most cases $m_t \simeq 40\,GeV$ and $m_H = 100\,GeV$) enter in the calculations. The results of the two schemes differ at the Born level (as a consequence of the two different $Z^0$ couplings of eqs. (19) and (20) in section 3.2) as well as in the QED and weak radiative corrections, but arrive at the same results once all corrections are taken into account. This is illustrated in Table 2 for the observable charge asymmetry in the reaction $e^+e^- \to \mu^+\mu^-$ at two typical PETRA energies of



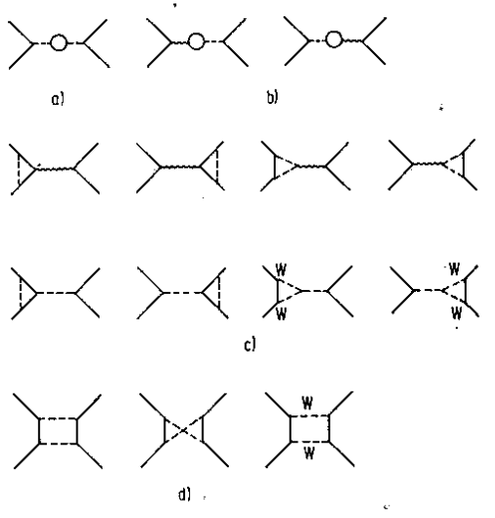


Figure 10: Some first order weak correction diagrams for the reaction $e^+e^- \to f\bar{f}$. a) $Z^0$ self energy, b) $\gamma - Z^0$ self energy, c) vertex corrections, d) box diagrams

Table 2: Effects of radiative corrections on the observable charge asymmetry $A_{\mu\mu}$[%] in the reaction $e^+e^- \to \mu^+\mu^-$ at $\sqrt{s} = 34.5\,GeV$ and $44.0\,GeV$. Event selection criteria correspond to a polar angle acceptance $|\cos\theta_\mu| < 0.80$, acollinearity angle $\xi < 10^0$, radiated photon energy $k < \sqrt{s}/4$. Values are given for the on-shell scheme and the $Z$-mass scheme using $m_Z = 92\,GeV$ and $\sin^2\theta_W = 0.23$

| | $\sqrt{s} = 34.5\,GeV$ renormalization scheme | | $\sqrt{s} = 44.0\,GeV$ renormalization scheme | |
|---|---|---|---|---|
| | on-shell | $Z$-mass | on-shell | $Z$-mass |
| Born term | −7.62 | −8.16 | −13.63 | −14.66 |
| + reduced QED | −5.80 | −6.31 | −11.82 | −12.86 |
| + full QED | −5.28 | −5.82 | −10.85 | −11.98 |
| + weak corr. | −5.89 | −5.86 | −11.93 | −11.89 |

$\sqrt{s} = 34.5\,GeV$ and $\sqrt{s} = 44\,GeV$ for 'reasonable' experimental cuts [11]. It turns out that at PETRA energies there is the accidental situation that the QED corrections to the photon Born term using the on-shell scheme (i.e. the $Z^0$ coupling of eq. (19)) coincide with the full corrections applied to the $Z^0$ diagrams. The small differences are below the experimental precision. Therefore it became customary that PETRA, PEP and TRISTAN experiments present 'lowest order data' with only 'reduced QED corrections' applied. This procedure need not to be applicable at higher energies, where different strategies have to be employed.

### 4.3 $e^+e^- \to e^+e^-$, $e^+e^-\gamma$

The first order radiative corrections to Bhabha scattering $e^+e^- \to e^+e^-$ are completely analogous to fermion pair production. There are twice as many diagrams, besides the $\gamma$ and $Z^0$ annihilation graphs for the $s$ channel a similar set of diagrams occur in the $t$ channel (see Figs. 8, 9). The calculations of the QED radiative corrections are again split into virtual and soft bremsstrahlung corrections, which by themselves are divergent but, when summed up, give finite results, and hard photon bremsstrahlung. 'Reduced QED corrections' to the $\gamma$ diagrams are the dominant part. QED corrections to the $Z^0$ graphs have been calculated and turn out to be less important. They are therefore not applied to the data. Also the first order weak corrections have been computed. In the on-shell scheme they are completely negligible at present energies and achieved experimental resolutions. Therefore all data are published as 'lowest order data' unfolded by detector acceptance and 'reduced QED corrections'.

### 4.4 Event generators

Experimental selection criteria cannot easily be translated into analytic cross section formulas. Therefore a tremendous amount of work has been done to provide Monte Carlo event generators for the previously discussed elementary reactions including first order radiative corrections. Event generators exist for the two photon production $e^+e^- \to \gamma\gamma$ [12], for lepton pair production $e^+e^- \to \mu^+\mu^-$ [13] and $e^+e^- \to \tau^+\tau^-$ [14], which can be easily modifyed to quark pair production, and Bhabha scattering $e^+e^- \to e^+e^-$ [15]. In general they contain the 'reduced QED corrections', the 'full QED corrections' and the most important weak corrections, adequate for energies below the $Z^0$ resonance. Recently also programs including weak corrections for high precision electroweak tests around the $Z^0$ pole are being developed.

Contrary to analytic formulas the Monte Carlo event generators cannot be exact in all regions of the phase space. For example the cross sections exhibit extremely peaking structures in the soft photon limit $k \to 0$ and in collinear configurations where a soft photon is emitted in the direction of the charged fermions. Hard bremsstrahlung peaks also occur in fermion production and Bhabha scattering from $1/s'$, $1/t$ and $1/t'$ terms. None of the peaks get singular. However, numerical methods have to be devised in order to perform the integrations with the required precision.

An example where finer details of an event sample cannot be reproduced is the



photon energy spectrum. Within an event generator all events with a soft photon below a certain energy threshold $k < k_0$ (typically below 1% of the beam energy) are simulated as two body reactions, while for photons with $k > k_0$ three body final states are produced. Thus there appears a discontinuity in the photon spectrum which also reflects in the acollinearity angle distribution $\xi$ of the final state particles for very small values of $\xi$. However, for all practical purposes it is possible to avoid the peaking regions and limitations of the event generators. Thus the Monte Carlo event generator programs are of prime importance and allow to simulate the experiments as precisely as possible and necessary and extract from the data cross sections which can be confronted with QED and the electroweak standard theory.

In addition to the first order radiative correction generators of the basic two body reactions there exist satisfactory approximations to higher order four particle final states such as $e^+e^- \to f\bar{f}\gamma\gamma$ and four lepton final states $e^+e^- \to e^+e^-l^+l^-(\gamma)$ [16], which are interesting by themselves and have to be accounted for as background sources to the two body reactions.

## 5 Photon–photon collision cross sections

The four lepton production $e^+e^- \to e^+e^-l^+l^-$ can be envisaged as a two stage process. In the first step the initial electron and positron radiate virtual photons, which in the second step produce the final state $X$, in this case the lepton pairs $\gamma\gamma \to X \to l^+l^-$. In this picture it is obvious that $e^+e^-$ colliders are an ideal place to study photon–photon collisions. The Feynman diagram and relevant kinematic quantities for the reaction $e^+e^- \to e^+e^-l^+l^-$ are shown in Fig. 11. It is a pure QED process of order $\alpha^4$ and the cross section can be calculated in a straighforward but tedious way, giving lengthy and not very handy formulas.

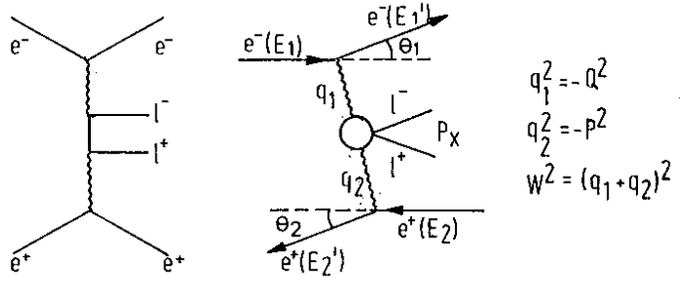


Figure 11: The two–photon process $e^+e^- \to e^+e^-X \to e^+e^-l^+l^-$. Feynman diagram and kinematics

Fortunately simple and reliable approximations exist which will be used in the

following discussion. A very successful approach is the Weizsäcker-Williams approximation. The spectrum of the bremsstrahlung photons is given by

$$\frac{dN}{d\omega} = \frac{\alpha}{2\pi}\frac{1+(1-\omega)^2}{\omega}\eta\,, \tag{37}$$

where $\omega = E_\gamma/E$ is the fractional energy of the photon in terms of the beam energy $E$. The function $\eta$ accounts for the direction of the electron/positron and depends on the momentum transfer $q^2$ or virtual mass of the photon. The momentum transfer is experimentally controlable. A vanishing momentum transfer, $q^2 \to 0$, means that the electron/positron is not deflected, $\theta \simeq 0^0$, this is called the no-tag case. If the momentum transfer becomes large, $q^2 \neq 0$, the electron/positron will be scattered at a polar angle $\theta$. If $\theta > \theta_{min}$ falls inside the detector acceptance the so called tag case occurs. For small angles $-q^2 = Q^2 \simeq E\,E'\,\theta^2$ and the function $\eta$ takes for the two situations the form

$$\begin{aligned}\eta &= \ln\frac{E^2}{m_e^2} && \text{no}-\text{tag}\,,\\ &= \ln\frac{Q^2}{Q^2_{min}} = \ln\frac{\theta^2}{\theta^2_{min}} && \text{tag}\,.\end{aligned}$$

The convoluted photon spectra at a given invariant $\gamma\gamma$ mass $W$ or fractional mass $\tilde{s} = W/\sqrt{s}$ can be translated into a $\gamma\gamma$ luminosity function $L_{\gamma\gamma}$

$$\begin{aligned}\frac{d\,L_{\gamma\gamma}(\tilde{s})}{d\,\tilde{s}} &= \left(\frac{\alpha}{\pi}\right)^2\frac{f(\tilde{s})}{\tilde{s}}\eta^2\,, \qquad (38)\\ f(\tilde{s}) &= (2+\tilde{s}^2)^2\ln\frac{1}{\tilde{s}} - (1-\tilde{s}^2)(3+\tilde{s}^2)\,.\end{aligned}$$

The observable two–photon cross section can then be written as a convolution of the cross section $\sigma_{\gamma\gamma}$ for the sub-process $\gamma\gamma \to l^+l^-$ with the $\gamma\gamma$ luminosity $L_{\gamma\gamma}$

$$\sigma(e^+e^- \to e^+e^-l^+l^-) = \int L_{\gamma\gamma}(\tilde{s})\,\sigma_{\gamma\gamma}(\tilde{s})\,d\tilde{s}\,. \tag{39}$$

First the no-tag case will be considered, where both photons are nearly on mass shell, i.e. $q_1^2 \to 0$ and $q_2^2 \to 0$. Using for the specific sub process $\gamma\gamma \to \mu^+\mu^-$ the very rough approximation $\sigma_{\gamma\gamma} = 4\pi\alpha^2/W^2$ the total cross section for $e^+e^- \to e^+e^-\mu^+\mu^-$ becomes

$$\sigma(e^+e^- \to e^+e^-\mu^+\mu^-) = \frac{8\,\alpha^4}{\pi}\ln^2\left(\frac{E}{m_e}\right)\ln\left(\frac{E}{m_\mu}\right)\frac{1}{m_\mu^2}\,. \tag{40}$$

The surprising result is that the $\mathcal{O}(\alpha^4)$ photon–photon collision cross section rises logarithmically with the beam energy and becomes even larger then the $\mathcal{O}(\alpha^2)$ annihilation cross section at not too high energy. This is shown in Fig. 12, where the total cross sections for one-photon and two-photon $\mu$ pair production are compared.

It should be noted, however, that most of the cross section is unobservable in the experiments. First, the initial state photons are strongly aligned along the beam



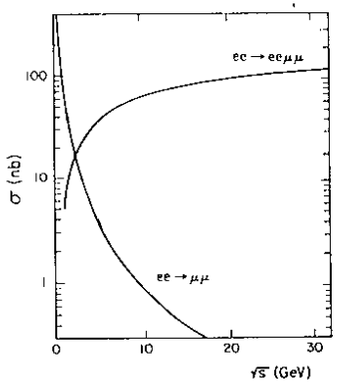


Figure 12: The two–photon cross section for $e^+e^- \to e^+e^-\mu^+\mu^-$ compared to the annihilation cross section for $e^+e^- \to \mu^+\mu^-$ as a function of the centre of mass energy $\sqrt{s}$

direction and the $\gamma\gamma$ centre of mass system is moving along that direction. Second, the lepton pair production cross section $\gamma\gamma \to l^+l^-$, which is obviously the reverse of $e^+e^- \to \gamma\gamma$ production discussed in section 3.1 modified according to the involved leptons, is in the $\gamma\gamma$ centre of mass system strongly peaked along the photon direction with a polar angle $\theta^*$ distribution of

$$\frac{d\sigma(\gamma\gamma \to l^+l^-)}{d\cos\theta^*} \propto \frac{1+\cos^2\theta^*}{\sin^2\theta^*}\,. \tag{41}$$

The observable cross section is therefore only a few percent of the total cross section falling rapidly with the $\gamma\gamma$ centre of mass energy $W$. The Weizsäcker-Williams approximation overestimates the exact luminosity calculations by about 20% for $\tilde{s} < 0.8$, but reproduces the shape of the distribution well.

Now the tag case will be discussed. As explained above one can tune the masses of the photons by a measurement of the electron/positron scattering angle $\theta$ . The limit of $q_1^2$ large and $q_2^2 \to 0$ can be interpreted as deep inelastic electron scattering off an (almost) real photon target $e\gamma \to e\mu^+\mu^-$. The factorization into a $\gamma\gamma$ cross section and the $\gamma\gamma$ luminosity function is no longer valid. Instead one has to sum over the transverse and longitudinal photon polarizations weighted with the appropriate spin densities. The formalism is completely analoguous to deep inelastic lepton nucleon scattering. The differential cross section for $e\gamma$ scattering is parametrized by two structure functions $F_1$ and $F_2$ as [17]

$$\frac{d^2\sigma}{dx\,dQ^2} = \frac{4\pi\alpha^2}{Q^4\,x}\left\{(1-y)\,F_2 + x\,y^2\,F_1\right\}\,, \tag{42}$$

with the kinematic variables

$$\begin{aligned}Q^2 &= 4\,E\,E'\sin^2\frac{\theta}{2}\,,\\ x &= \frac{Q^2}{Q^2+W^2}\,,\\ y &= 1-\frac{E'}{E}\cos^2\frac{\theta}{2}\,.\end{aligned}$$

$E'$ is the energy of the scattered electron/positron and $\theta$ its scattering angle. The structure functions depend on the scaling variables $x$ and $Q^2$. $F_1$ is under standard experimental conditions not accessible since the coefficient $x\,y^2$ is too small. The photon structure function $F_2(x,Q^2)$ describes the pointlike coupling of the photon to the muon pair. It is calculable in QED [17] and is for $W^2 \gg 4\,m_\mu^2$ given by

$$F_2(x,Q^2) = \frac{\alpha}{\pi}\,x\left\{\left(x^2+(1-x)^2\right)\,\ln\frac{Q^2\,(1/x-1)}{m_\mu^2} - 1 + 8\,x\,(1-x)\right\}\,. \qquad (43)$$

The above formulas can be easily applied to other leptons with obvious modifications regarding the lepton mass. For quarks an additional factor $N_q^c\,\sum_q Q_q^4$ has to be added containing a colour factor $N_q^c = 3$ and the quark charges $Q_q$. The corresponding hadronic structure function is theoretically less well known and is an interesting object for QCD studies. The leptonic reactions $e^+e^- \to e^+e^-e^+e^-$ and $e^+e^- \to e^+e^-\mu^+\mu^-$ serve as prototypes for QED photon–photon collisions. Only if they are understood one can hope to learn something from two-photon quark pair or hadron production.

Photon–photon collisions are extremely difficult to analyze without detailed acceptance simulation of the detector, because of the moving centre of mass system and the rapidly falling $\gamma\gamma$ luminosity. Monte Carlo event generators for four lepton production $e^+e^- \to e^+e^-l^+l^-(\gamma)$ have been provided [16] without and with hard photon radiation. The lepton event generators have also been extended to two-photon production of quarks.

# 6 Experiments

One of the most critical design parameter of a collider is the luminosity $\mathcal{L}$ $[cm^{-2}\,s^{-1}]$ determining the rate at which an experiment will take data. The number of recorded events for a given reaction is

$$N = \sigma\cdot\epsilon\cdot\int\mathcal{L}\,dt\,.$$

Here $\sigma$ is the observable cross section, $\epsilon$ an efficiency factor and $\int\mathcal{L}\,dt$ the time integrated luminosity of the $e^+e^-$ collider.

In the past decade the most significant $e^+e^-$ experiments to test QED and the electroweak theory have been performed at the storage rings PETRA (at DESY in Hamburg) and PEP (at SLAC in Stanford).

PETRA has been operated from 1978 till 1986 and covered a large centre of mass energy region from 12 to 46.8 $GeV$, thereby extending the energy scale of previous QED tests from SPEAR (SLAC) and DORIS (DESY) by almost an order of magnitude. Much of the data were taken in a scanning mode, where the energy was varied in small step sizes of 20 or 30 $MeV$. This mode of operation was motivated by the search for new open quark or bound quark states, notably the top quark. Five



experiments have been operated during the years: CELLO which succeeded PLUTO, JADE, MARK J and TASSO. A typical history of an experiment in terms of luminosity and energy is shown in Fig. 13. As can be seen the energy was continuously upgraded, only the last year run was at a fixed energy of 35.0 $GeV$. Each experiment has collected a total integrated luminosity of about 250 $pb^{-1}$. For the analysis energy intervals were grouped together. Statistically significant data samples are available for average energies around $\sqrt{s} \sim 14\,GeV$, 22 $GeV$, 35 $GeV$ ($\sim 180\,pb^{-1}$), 38 $GeV$ ($\sim 15\,pb^{-1}$), and 44 $GeV$ ($\sim 40\,pb^{-1}$).

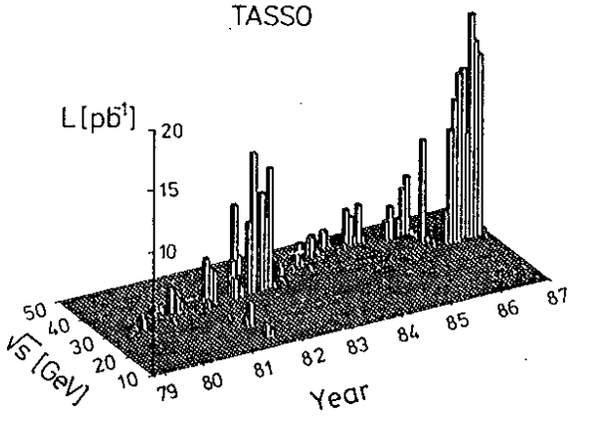


Figure 13: History of the TASSO experiment in terms of accumulated integrated luminosity as function of the centre of mass energy and date of running

The storage ring PEP operated from 1980 on at a fixed energy of $\sqrt{s} = 29\,GeV$. The experiments HRS, MAC, MARK II and TPC (and previously DELCO and ASP) took data until the end of 1986 and have each collected about $220 - 300\,pb^{-1}$ of integrated luminosity, comparable with what has been accumulated by the PETRA experiments. The lower energy yields larger event samples due to the $1/s$ dependence of the cross sections. On the other hand the sensitivity to QED and to the electroweak interference as well as to phenomena beyond the standard theory is rising with $s$, in fact sometimes faster than linear in $s$. Larger effects also mean that systematic experimental biases become less important. In this respect the PETRA experiments were in a more favourable position than the PEP experiments.

Immediately after the PETRA shut down at the end of 1986 the TRISTAN storage ring at KEK, Japan, started its physics program at energies between 50 and 60 $GeV$. By the end of 1988 a maximum energy of 60 $GeV$ was reached and the experiments AMY, TOPAZ and VENUS have reported results based on an integrated luminosity of about 20 $pb^{-1}$ for each experiment. The upgrade program foresees to extend the energy range up to 66 $GeV$.

In 1989 the two new colliders SLC (at SLAC) and LEP (at CERN) came into

operation working in the energy region around $\sqrt{s} \simeq m_Z$. They aim at studying the properties of the $Z^0$ resonance with high precision ('$Z^0$ factories'). The MARK II experiment at SLC has gathered the first $Z^0$ events in the spring of 1989, while the LEP experiments just recorded the first events in summer 1989.

Most $e^+e^-$ experiments have been built as general multi-purpose detectors in order to exploit the large variety of physics questions. They should be able to detect the different topologies of low multiplicity (leptons, photons) and high multiplicity (hadrons) events from conventional $\gamma$ and $Z^0$ exchange, from two-photon processes which are boosted along the beam directions and unexpected exotic reactions. This requires hermetically closed '$4\pi$ detectors' with momentum analysis of charged particles through bending in a magnetic field and particle identification of electrons, muons and photons. Charged track measurements are usually provided by drift chambers over a solid angle of more than 80 % of $4\pi$, whereas electromagnetic calorimetry by lead sandwhich or lead glass counters extends up to 95 % of the solid angle. Muon identification is typically done over 80 % of $4\pi$ with wire chambers situated inside or behind the iron magnetic flux return which absorbs the hadrons. The luminosity is monitored by shower counters using the high rate Bhabha scattering at very low angles ($\theta \sim 30\,mrad$).

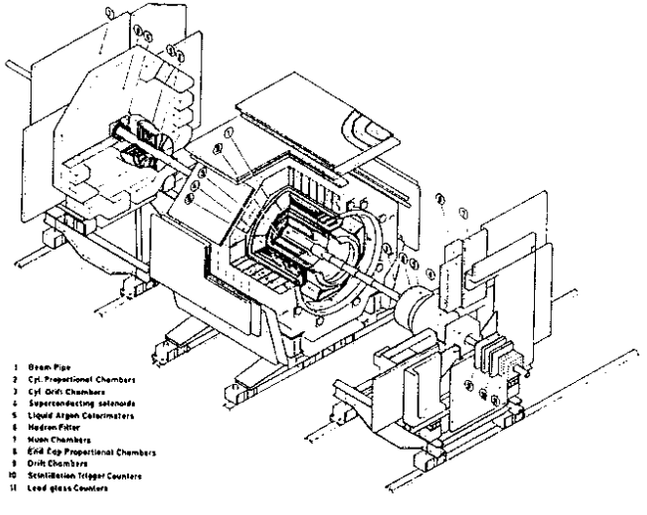


Figure 14: The CELLO detector at the PETRA $e^+e^-$ storage ring

A typical representative is the CELLO detector at PETRA shown in Fig. 14. The central detector consists of drift and proportional chambers placed inside a thin superconducting coil (0.47 radiation length thick, 1.5 m diameter) providing a magnetic field of 1.3 Tesla. The coverage extends over 91% of $4\pi$ and the achieved momentum resolution is $\sigma/p = 0.013\,p\,[GeV]$ at $\theta = 90^0$. Outside the coil is a 20



radiation length thick liquid argon electromagnetic calorimeter (octagonal barrel and end caps) covering 86% of the solid angle. A fine grained strip read out with 19 samplings in depth allows electron/photon identification with an energy resolution of $\sigma/E = 0.13/\sqrt{E\,[GeV]}$ and an angular resolution of $4\,mrad$. Muon detection is done with one set of planar wire chambers behind the flux return (80 cm iron or 5.5 nuclear interaction lengths at $\theta = 90^0$) over 92% of $4\pi$.

The limited space here does not permit to go into more details and to present other detectors as well. More information can be found in the original literature or, e.g., in the review article on $e^+e^-$ detectors by Lynch in ref. [18]. In the following the general features of measurement and analysis of the basic $e^+e^-$ reactions will be briefly described.

The experimental signature for the reaction $e^+e^- \to \gamma\gamma$ is two energetic clusters in the electromagnetic calorimeter with no additional charged track in the detector. The two clusters should point to the common interaction region and are required to be back-to-back within a typical acollinearity angle of $\xi < 20^0$. The energy of each cluster should be close to the beam energy, which poses no experimental problems since the resolution of shower counters improves with energy as $\sigma/E \sim 1/\sqrt{E}$. The most serious background comes from Bhabha scattering $e^+e^- \to e^+e^-$, where both particles leave no signature in the tracking chambers. These inefficiencies have to be corrected for in the analysis. To further reduce background from e.g. $e^+e^- \to e^+e^-\pi^0$, $e^+e^-\eta$ with $\pi^0 \to \gamma\gamma$ and $\eta \to \gamma\gamma$ and undetected $e^\pm$ a typical cut on $E_\gamma > 0.25\,E_{beam}$ is applied. Multiple photon emission at large polar angles is in most cases easily detected through the fine spatial granularity of the electromagnetic calorimeter.

The experimental signature for the reaction $e^+e^- \to \mu^+\mu^-$ is two oppositely charged tracks emerging from a common interaction vertex. The tracks have to be acollinear with typical cuts of $\xi < 20^0$. The particles are identified as muons by their penetration through iron of about 6 - 8 interaction lengths, which efficiently absorbs all other particles. The momentum is either measured by drift chambers within a solenoidal magnetic field with a typical resolution of $\sigma/p \sim 1\text{–}2\,\%\cdot p\,[GeV]$ or through bending in magnetized iron (MAC, MARK J) with a resolution of $\sigma/p \sim 30\%$. The achieved resolutions are in general sufficient to determine the charge of the muon, with a probability of at most a few percent that both tracks have a wrong charge assignment simultaneously. The experiments have shown in detailed investigations that the charge measurement is not affected by any instrumental polar angle dependent effects in a systematic way. The systematic uncertainties of the measured charge asymmetry are of the order of 0.5% or less. A typical momentum cut $p_\mu > 0.25\,p_{beam}$ reduces background from the two-photon reaction $e^+e^- \to e^+e^-\mu^+\mu^-$, cosmic rays (plus additional time of flight cuts) and $\tau$ pair production where both particles decay into $\tau \to \mu\nu_\mu\nu_\tau$ (branching ratio $17.8 \pm 0.4\,\%$). The residual background is less than a percent. The radiative process $e^+e^- \to \mu^+\mu^-\gamma$ with a photon at large polar angle is again detected with the help of the electromagnetic shower counters.

The reaction $e^+e^- \to \tau^+\tau^-$ at high energies has a very distinct signature. The decay multiplicities are small. The $\tau$ decays after a mean life time of $(3.04 \pm 0.09) \cdot 10^{-13}\,s$ either in a lepton plus two neutrinos or in one to three hadrons plus neutrino; decays into 5 or more charged particles are negligible. The topological branching fractions of the $\tau$ decaying into 1 charged particle plus neutrals (neutrinos, photons)

is 85.7 ± 0.4 % and of the $\tau$ decaying into 3 charged particles plus neutrals is 14.3 ± 0.4 %. At high energies the decay particles are boosted in a narrow cone around the original flight direction of the $\tau$. Requiring, as most experiments do, a one-prong decay recoiling against a narrow jet like three-prong decay with certain momentum and geometrical cuts leaves a very clean $\tau$ pair event sample without any particle identification. An example of such a topology is shown in Fig. 15. However, the price is that only a quarter of all decays are used. The background from low multiplicity hadron events, Bhabha events where an accompanying photon converts in the beam pipe into an $e^+e^-$ pair faking a three-prong jet, and the two-photon reaction $e^+e^- \to e^+e^-\tau^+\tau^-$ can be kept low, of the order of a few percent. In principle all $\tau$ decays can be used for analysis except those where both $\tau$ decay into electrons or muons, thereby raising the acceptable decay modes to about 90%. In this case, however, refined particle identification is mandatory. This has been achieved only by few experiments. Small corrections to the direction measurement have to be applied, since the momentum vector of the one- or three-prong decay does not coincide with the direction of the produced $\tau$.

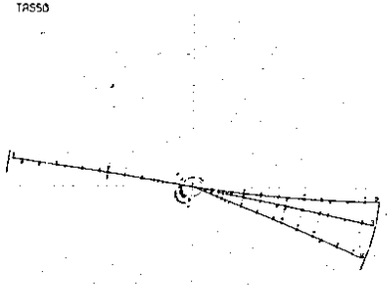


Figure 15: An $e^+e^- \to \tau^+\tau^-$ event observed in the TASSO detector at $\sqrt{s} = 35\,GeV$ (view perpendicular to the beams). The one-prong decay is identified as $\tau^- \to \mu^-\bar{\nu}_\mu\nu_\tau$, the three-prong decay as $\tau^+ \to (3\,hadrons)^+\nu_\tau\,(n\gamma)$

The reaction $e^+e^- \to e^+e^-$ has a signature very similar to the two photon pair production above, except that a charged track has to be associated with each calorimetric energy cluster. Geometrical matching requires that the charged track points to the centre of the energy cluster. If magnetic momentum analysis is available, a track momentum energy balance within the experimental resolutions is performed. Note that at high energies the energy measurement is superior to the momentum measurement. As mentioned previously the angular distribution in Bhabha scattering is extremely peaked in the forward direction, the differential cross section at $\cos\theta = +0.8$ is about 80 times larger than at $\cos\theta = -0.8$. This implies that extremely good momentum resolution is needed in order not to affect the angular distribution measurements in the backward region by charge confusion. Some experiments therefore prefer to show angular distributions folded around $\cos\theta = 0$. The selection criteria are typically an acollinearity cut of $\xi < 20^0$ and an energy cut for each particle of $E_e > 0.25\,E_{beam}$. The background from hadron production, $\tau$ pair production and two-photon reactions can be easily separated since almost all centre of mass energy is released in the electromagnetic calorimeter and well measured. A remaining small background comes from $e^+e^- \to \gamma\gamma$, where both photons convert in



the beam pipe into highly asymmetric $e^+e^-$ pairs. These effects have to be taken into account in the acceptance calculations. Since Bhabha scattering has by far the largest cross section of all reactions leading to two charged particles in the final state, the TASSO collaboration did an analysis without any particle identification. With somewhat more stringent selection criteria on high momentum acollinear two prong events, their Bhabha event sample contains about 5.5% overall background from $\mu$ and $\tau$ pairs. This background is statistically subtracted from the angular distribution, the correction reaching substantial values of about 25% in the backward region.

The experimental signature of the photon-photon reactions $e^+e^- \to e^+e^-l^+l^-$ ($l$ = $e$ or $\mu$) is two oppositely charged tracks which appear to be back-to-back (coplanar) in the plane perpendicular to the $e^\pm$ beams but are acollinear due to the moving $\gamma\gamma$ centre of mass system. The event selection is just opposite to the charged two-prong annihilation events, which are discriminated by requiring a minimum acollinearity angle in space and a cut on the maximum visible energy. Since the $\gamma\gamma$ luminosity drops rapidly with the $\gamma\gamma$ centre of mass energy the bulk of the events appears at low energies. Therefore the track momentum resolution poses no problems. Momentum balance in the plane perpendicular to the $e^\pm$ beam direction between the two charged tracks (and the electron/positron if it is tagged) assures that it is an exclusive process with no further undetected particles. A more severe problem is the electron and muon identification at low momenta around $1\,GeV$ against hadrons, which are copiously produced either directly or via resonance decays. A possible background comes from beam gas events where the electron/positron hits a nucleus inside the vacuum chamber thereby producing acoplanar low energy event topologies. But their interaction vertex is uniformly distributed along the beam direction and they can be statistically subtracted from the two-photon event sample.

# 7 Experimental tests of QED

In this section the experimental tests of QED will be discussed. It is divided in two particle final states, hard photon radiation processes and photon-photon collisions. Due to the overwhelming amount of material not all the beautiful experimental results can be presented. Instead a few examples are chosen which demonstrate the achievements of the experimental QED tests.

## 7.1 Two particle final states

### 7.1.1 $e^+e^- \to \gamma\gamma$

The reaction $e^+e^- \to \gamma\gamma$ provides the cleanest QED test at the one loop level, since hadronic vacuum polarization and electroweak effects only enter in the second order corrections. This process has been studied by many experiments.

Fig. 16 shows the differential cross section distributions at four energies and the total cross section integrated over $|\cos\theta| < 0.76$ between 12 and $44\,GeV$ from the JADE experiment. The agreement with QED is very good.

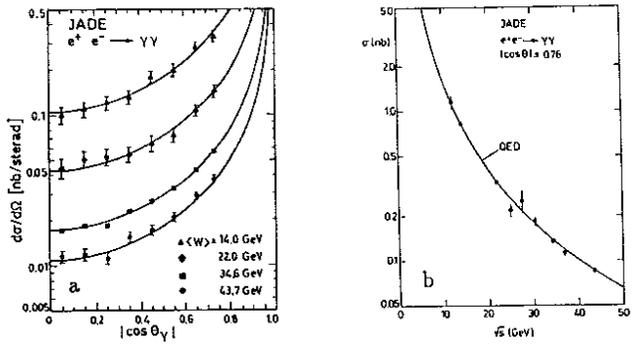


Figure 16: Cross section distributions for the reaction $e^+e^- \to \gamma\gamma$ from JADE. a) Differential cross sections at $\sqrt{s} = 14$, 22, 34.5 and 43.1 $GeV$, b) total cross section as a function of the energy. The curves show the QED prediction

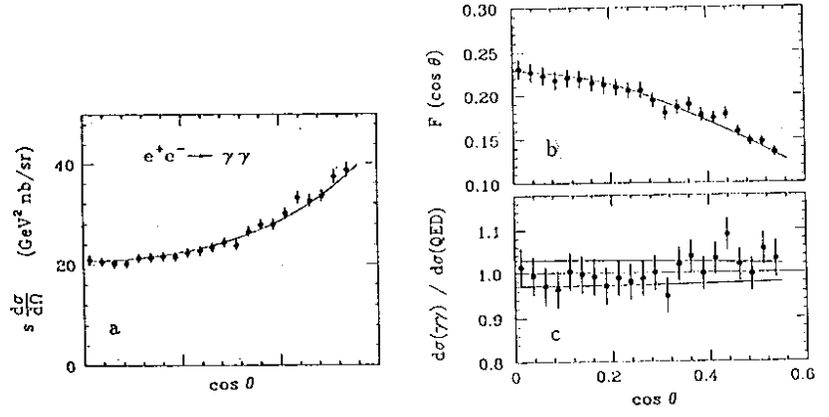


Figure 17: Cross section distributions for the reaction $e^+e^- \to \gamma\gamma$ from HRS at $\sqrt{s} = 29\,GeV$. a) The differential cross section, b) the differential cross section divided by the Bhabha cross section, c) the differential cross section divided by the QED cross section. The curves are the QED prediction, the upper and lower curves in c) represent experimental limits for $\Lambda > 59\,GeV$

The most precise measurement has been performed by the HRS collaboration, which collected 14880 $\gamma$ pairs at large angles $|\cos\theta| < 0.55$ at an energy of $\sqrt{s} = 29\,GeV$. The differential cross section is shown in Fig. 17a, and the same data normalized to the QED prediction are plotted in Fig. 17c. Each data point has an



error of about 4%, while the overall systematic uncertainty is 0.6%. The average value is very close to one with an overall error of less than 2%, significantly lower than the first order radiative corrections, which amount on average to about 8%. The measurement clearly demonstrates the necessity and correctness of the $\mathcal{O}(\alpha^3)$ QED calculations. In order to overcome the problems related to an absolute luminosity measurement the $\gamma\gamma$ data were compared bin by bin to a high statistics Bhabha event sample (84423 events) selected under similar conditions. This is shown in Fig. 17b, where the function $F(\cos\theta)$ represents the $\gamma\gamma$ angular distribution divided by the Bhabha cross section folded around $\cos\theta$ and corrected for small electroweak effects. In this quantity common systematic uncertainties cancel. As can be seen the agreement with QED is excellent. Defining $\Sigma$ as the integral of $F(\cos\theta)$ over $|\cos\theta| < 0.55$ a fit to the QED prediction yields

$$\frac{\Sigma^{meas}}{\Sigma^{QED}} = 1.007 \pm 0.009 \pm 0.008\,,$$

where the first error is statistical and the second systematic. This most precise measurement shows that $\mathcal{O}(\alpha^3)$ QED calculations have been experimentally tested at the level of one percent.

A compilation of results on $R_{\gamma\gamma} = \sigma^{meas}/\sigma^{QED}$ as a function of the centre of mass energy squared $s$ is shown in Fig. 18. All measurements confirm QED within a few percent.

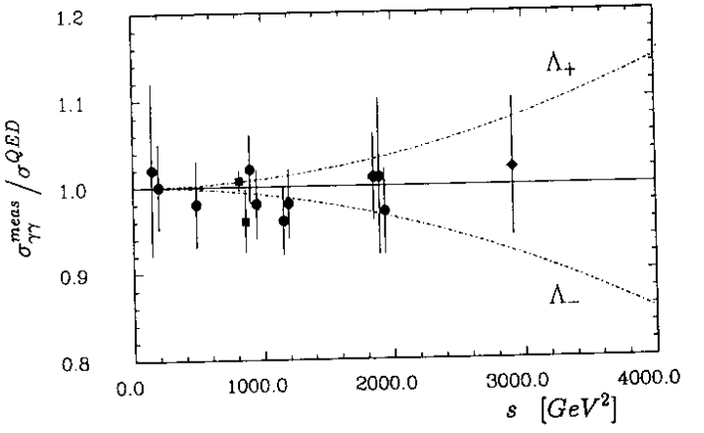


Figure 18: Cross sections normalized to QED for the reaction $e^+e^- \to \gamma\gamma$ as a function of the centre of mass energy squared $s$. Data are from PETRA (circles), PEP (squares) and TRISTAN (diamond) experiments. The full line shows the QED expectation, the dashed curves show the expected deviation from QED for cut-off parameters $\Lambda = 80\,GeV$

A quantitative non-gauge invariant formulation of a possible break down of QED

has been proposed by [19] long time before the invention of the electroweak theory. In this scheme the photon propagator is modified according to

$$\frac{1}{q^2} \rightarrow \frac{1}{q^2} - \frac{1}{q^2 - \Lambda^2} = \frac{1}{q^2}\left(1 - \frac{q^2}{q^2 - \Lambda^2}\right) ,$$

where the cut-off parameter $\Lambda$ can be interpreted as the mass of an additional heavy photon with coupling strength $\alpha$. For high values $\Lambda \rightarrow \infty$ the original theory is restored. Such a heavy photon would also modify the vertex and the fermion propagator.

All these contributions can be absorbed in a so-called form factor, which alters the observable differential cross section [20] of the reaction $e^+e^- \rightarrow \gamma\gamma$ as

$$\frac{d\sigma}{d\Omega} = \frac{\alpha^2}{s}\frac{1+\cos^2\theta}{\sin^2\theta}\left(1 \pm \frac{s^2}{2\,\Lambda_\pm^4}\frac{\sin^4\theta}{1+\cos^2\theta}\right) . \qquad (44)$$

The term with $\Lambda_-$ has no simple physical interpretation, but is added for convenience to also account for a lower cross section.

Another possible deviation from QED could arise through the exchange of a heavy or excited electron $E^*$ with mass $m^*$ and coupling strength $\lambda e$. Electromagnetic current conservation allows only a coupling via the magnetic moments with the interaction Lagrangian

$$\mathcal{L}_{int} = \frac{\lambda\, e}{2\, m^*}\bar{\psi}^{(*)}\,\sigma_{\mu\nu}\,F^{\mu\nu}\,\psi ,$$

where $\psi^{(*)}$ is the Dirac field of the spin 1/2 heavy electron, $\sigma_{\mu\nu} = i/2\,(\gamma_\mu\gamma_\nu - \gamma_\nu\gamma_\mu)$ and $F^{\mu\nu}$ is the elctromagnetic field tensor. Replacing the mass by $\Lambda$ and assuming $\lambda = 1$ the modified cross section becomes

$$\frac{d\sigma}{d\Omega} = \frac{\alpha^2}{s}\frac{1+\cos^2\theta}{\sin^2\theta}\left(1 \pm \frac{s^2}{2\,\Lambda_\pm^4}\frac{\sin^4\theta}{1-\cos^2\theta}\right) . \qquad (45)$$

Again the term proportional to $\Lambda_-$ is introduced for convenience to allow for a lower cross section.

Both form factor extensions to the cross section for $e^+e^- \rightarrow \gamma\gamma$ vary as $s^2/\Lambda^4$ and are identical at $\theta = 90^0$, where the sensitivity reaches its maximum. In the static limit the modified photon propagator can be interpreted as a modification of the r dependence of the Coulomb potential $1/r \rightarrow 1/r\,(1 - e^{-\Lambda r})$, i.e. the cut-off parameter $\Lambda$ is a measure of the pointlike nature of the $e\gamma$ interaction. In the second case the derived $\Lambda$ values set limits on the mass of an additional heavy electron. Most experiments analyze their data using eq. (45) and quote lower limits on $\Lambda_\pm$. However, the difference with eq. (44) is small, of the order of a few GeV.

As an example Fig. 17b shows the effect on the differential cross section for the lower limits (95% confidence level) of $\Lambda_+ > 59\,GeV$ and $\Lambda_- > 59\,GeV$ derived by the HRS experiment. The results from other experiments on the cut-off parameters $\Lambda$ are summarized in Table 3. The sensitivity is experimentally limited by the systematic error of the luminosity measurement (typically 3%) but rises with the centre of mass energy. This is evident from the higher values obtained by the TRISTAN



experiments at $\sqrt{s} \simeq 55\,GeV$, although they are less precise and have only a tenth of the luminosity compared to the high precision HRS data at $\sqrt{s} = 29\,GeV$. The effect of a hypothetical cut-off parameter of $\Lambda = 80\,GeV$ can also be seen in the total cross section data of Fig. 18.

Table 3: Lower limits (95 % confidence level) on QED cut-off parameters for the reaction $e^+e^- \rightarrow \gamma\gamma$

| Experiment | $\Lambda_+$ [GeV] | $\Lambda_-$ [GeV] |
|---|---|---|
| HRS [21,22] | 59 | 59 |
| MAC [23] | 66 | 67 |
| CELLO [24] | 84 | 44 |
| JADE [25] | 66 | 75 |
| MARK J [26] | 70 | 70 |
| PLUTO [27] | 46 | 36 |
| TASSO [28] | 61 | 56 |
| AMY [29] | 65 | — |
| TOPAZ [30] | 94 | 59 |
| VENUS [31] | 81 | 82 |

In summary QED is well tested up to $\mathcal{O}(\alpha^3)$ in the reaction $e^+e^- \rightarrow \gamma\gamma$ at the level of one percent. Lower limits on the cut-off parameters of $\Lambda_+ > 94\,GeV$ and $\Lambda_- > 82\,GeV$ have been obtained excluding a heavy electron of this mass.

### 7.1.2 $e^+e^- \rightarrow e^+e^-$

Bhabha scattering $e^+e^- \rightarrow e^+e^-$ serves two purposes. At small scattering angles or low momentum transfers, where QED is well established, it serves as a luminosity monitor with high rates, while at large angles or high momentum transfers tests of QED and the electroweak theory can be performed.

The precision of the luminosity determination is limited by systematic effects, which are caused by the steep rise of the angular distribution and the non perfect knowledge of the geometrical acceptance of the luminosity counters. The systematic uncertainties typically amount to 2 - 4 %.

Wide angle measurements of $e^+e^- \rightarrow e^+e^-$ have been performed by several experimental groups. An example of the differential cross section at $\sqrt{s} = 34.6\,GeV$ from the MARK J collaboration is shown in Fig 19. The detector covers polar angles of $12^0 < \theta < 168^0$, but, due to the lack of charged particle momentum analysis, the data are folded around $\theta = 90^0$. Another example is shown in Fig 20a, where the differential cross sections measured over $-0.8 < \cos\theta < 0.8$ at energies between $\sqrt{s} = 14$ and $43.6\,GeV$ by the TASSO collaboration are displayed.

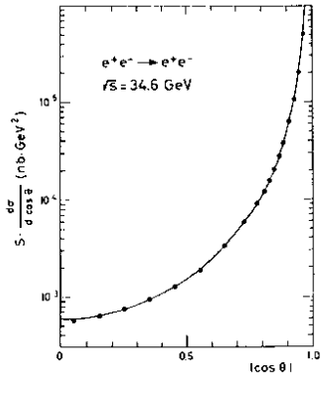


Figure 19: Differential cross section for the reaction $e^+e^- \rightarrow e^+e^-$ from MARK J at $\sqrt{s} = 34.6\,GeV$. The curve shows the QED prediction

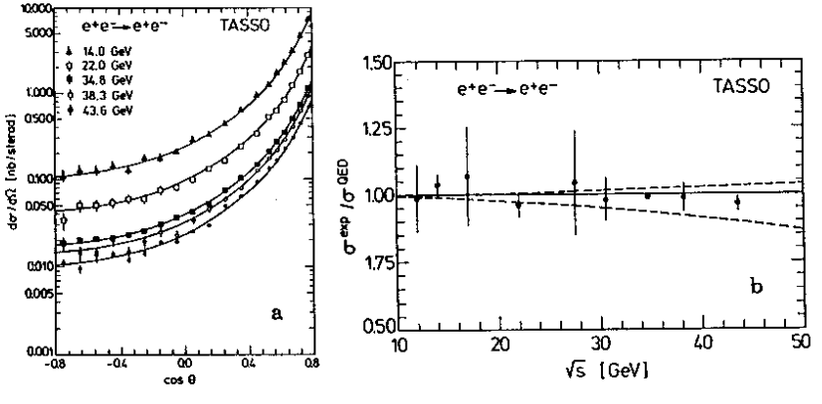


Figure 20: Cross section measurements for the reaction $e^+e^- \rightarrow e^+e^-$ from TASSO. a) Differential cross sections at $\sqrt{s} = 14$, 22, 34.8 and $43.6\,GeV$, b) total cross section integrated over $|\cos\theta| < 0.8$ divided by QED as a function of the centre of mass energy. The full curves show the QED prediction, the dashed curves show the deviation from QED for cut-off parameters $\Lambda_+ = 370\,GeV$ and $\Lambda_- = 190\,GeV$



At first sight Bhabha scattering seems to be well described by QED. A closer look at the data is provided by plotting the ratio of the measured over the QED predicted differential cross sections on a linear scale, as shown for some experiments in Fig. 21. Although in general good agreement with QED, the data are slightly better described if electroweak effects are included. To prove the presence of the small electroweak contributions is just marginally feasible for most experiments. Nevertheless, the measurements put stringent bounds on the parameters of the standard theory.

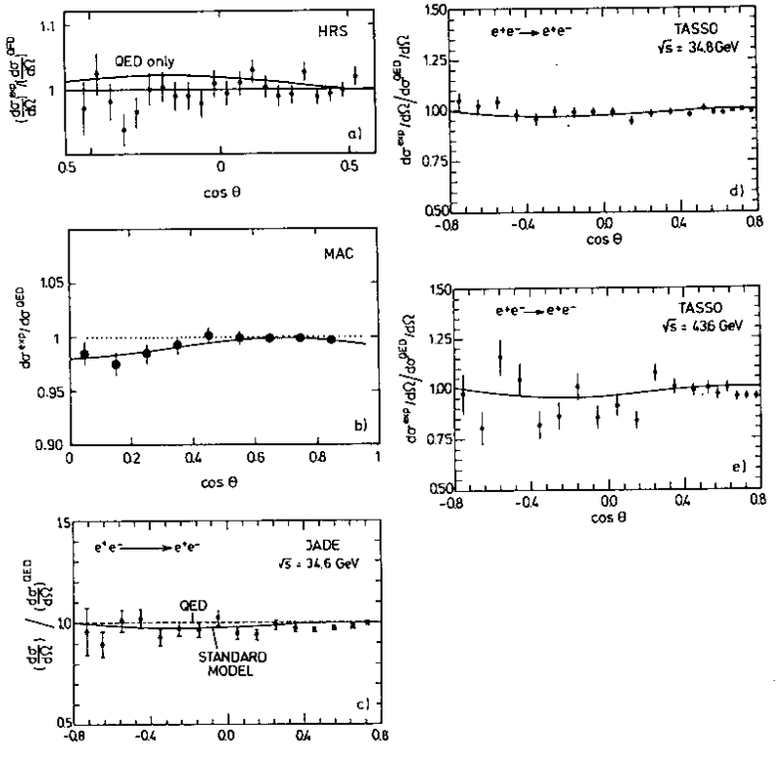


Figure 21: Differential cross section measurements for the reaction $e^+e^- \rightarrow e^+e^-$ divided by QED. a) HRS at $\sqrt{s} = 29\,GeV$ normalized to QFD, b) MAC at $\sqrt{s} = 29\,GeV$, c) JADE at $\sqrt{s} = 34.5\,GeV$, d) TASSO at $\sqrt{s} = 34.8\,GeV$, e) TASSO at $\sqrt{s} = 43.6\,GeV$. The curves show the QFD prediction

In order to perform quantitative tests of QED one can either use the total cross section, which is dominated by the forward region with negligible electroweak contributions, or apply small electroweak corrections to the differential cross sections. Fig.

20b shows the total Bhabha cross section integrated over $|\cos\theta| < 0.8$ as a function of energy from the TASSO experiment. The agreement with $\mathcal{O}(\alpha^3)$ QED calculations is at the level of 3% up to energies of $\sqrt{s} = 44\,GeV$.

In pure QED a breakdown can be formulated by inserting form factors

$$F(q^2) = 1 \mp \frac{q^2}{q^2 - \Lambda_\pm^2} \tag{46}$$

at the time-like, $q^2 = s$, and space-like, $q^2 = t = -s/2\,(1 - \cos\theta)$, vertices, which leads to the modified differential cross section

$$\frac{d\sigma}{d\Omega} = \frac{\alpha^2}{2\,s}\left\{\left(\frac{s}{t}\right)^2 F(t)^2 + \left(\frac{t}{s}\right)^2 F(s)^2 + \left(1+\frac{s}{t}\right)^2\left(1+\frac{t}{s}\right)^2\left(\frac{s}{t}F(t) + F(s)\right)^2\right\}. \tag{47}$$

The space-like, time-like and interference terms are apparent. Note that in Bhabha scattering the sensitivity is proportional to $q^2/\Lambda^2$. The data are analyzed after applying the small electroweak standard theory corrections (assuming $\sin^2\theta_W = 0.23$ and $m_Z = 92\,GeV$) and any residual deviation is attributed to the QED cut-off parameters $\Lambda$. The results of such fits are summarized in Table 4. Again the lower bounds are limited by systematic uncertainties of the luminosity and rise with the centre of mass energy. Lower limits of $\Lambda_+ > 435\,GeV$ and $\Lambda_- > 590\,GeV$ have been obtained. The effect of QED cut-off parameters on the total cross section can also be seen in Fig. 20b for the TASSO data.

Table 4: Lower limits (95 % confidence level) on QED cut-off parameters for the reaction $e^+e^- \to e^+e^-$

| Experiment | $\Lambda_+$ [GeV] | $\Lambda_-$ [GeV] |
|---|---|---|
| HRS [32,22] | 154 | 220 |
| MAC [33] | 256 | 179 |
| CELLO [34] | 83 | 155 |
| JADE [35] | 267 | 200 |
| MARK J [36] | 173 | 177 |
| PLUTO [37] | 162 | 184 |
| TASSO [38] | 435 | 590 |
| AMY [29] | 154 | 342 |
| TOPAZ [30] | 115 | 236 |
| VENUS [39] | 180 | 255 |

To summarize Bhabha scattering experiments are well described by $\mathcal{O}(\alpha^3)$ QED calculations at the level of a few percent with first hints of electroweak contributions. Lower limits on QED cut-off parameters $\Lambda$ exceed 400 GeV, which can be interpreted that the $ee\gamma$ interaction behaves as pointlike down to distances of less than $10^{-16}\,cm$.



### 7.1.3 $e^+e^- \to \mu^+\mu^-$ and $e^+e^- \to \tau^+\tau^-$

The lepton pair production reactions $e^+e^- \to \mu^+\mu^-$ and $e^+e^- \to \tau^+\tau^-$ are mediated at high energies through $\gamma$ and $Z^0$ annihilation diagrams. As discussed in section 3.2 their interference leads to considerable forward backward asymmetries, thus the differential cross section measurements are not suited for QED tests. However, at the energies considered here the total cross section can be well described by QED alone, because the electroweak interference effects cancel after integration over the polar angle. The weak contributions are expected to be very small due to the fact that the electron, muon and tau vector couplings are close to zero in the standard theory (see section 3.2).

The $\mathcal{O}(\alpha^3)$ radiative corrections are experimentally verified, as shown e.g. in Fig. 22 for the acollinearity angle distribution of $\mu$ pair production measured by MARK J. Data and QED simulations agree up to very large acollinerity angles. For the total cross section measurements the first order virtual and bremsstrahlung radiative corrections are of the order of 10%, depending on the selection criteria.

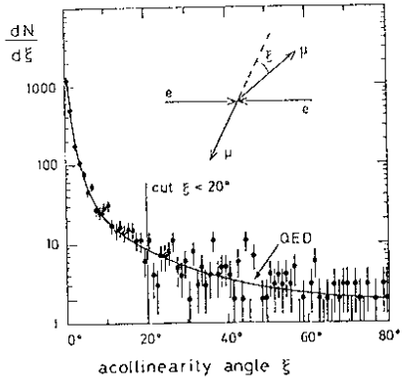


Figure 22: Acollinearity angle distribution for the reaction $e^+e^- \to \mu^+\mu^-$ by MARK J at $\sqrt{s} = 34.6\,GeV$. The curve shows the QED prediction

The $e^+e^- \to \mu^+\mu^-$ and $e^+e^- \to \tau^+\tau^-$ total cross sections normalized to the asymptotic QED prediction, $R_{\mu\mu,\tau\tau} = \sigma^{\mu\mu,\tau\tau}/\sigma^0$ with $\sigma^0 = 4\,\pi\,\alpha^2/3\,s$, are displayed in Fig. 23 as a function of the centre of mass energy squared. For both reactions the measured $R$ values are close to one with partially substantial errors. In the larger data samples the errors are dominated by systematic uncertainties on the luminosity of the order of 3 - 5 %. In addition $\tau$ pairs suffer from lower statistics and uncertainties in the decay branching ratios. The measurements are certainly consistent with QED, which is within the presently achieved accuracy practically indistinguishable from the QFD prediction. Only at TRISTAN energies around $s = \simeq 3000\,GeV^2$ deviations of a few percent are expected. The rise is due to the purely weak terms in the cross section formula of eq. (18). However, the statistical significance of the data is still unsufficient to observe weak contributions to the total leptonic cross sections.

Within QED any deviation is parametrized by a time-like polar angle independent

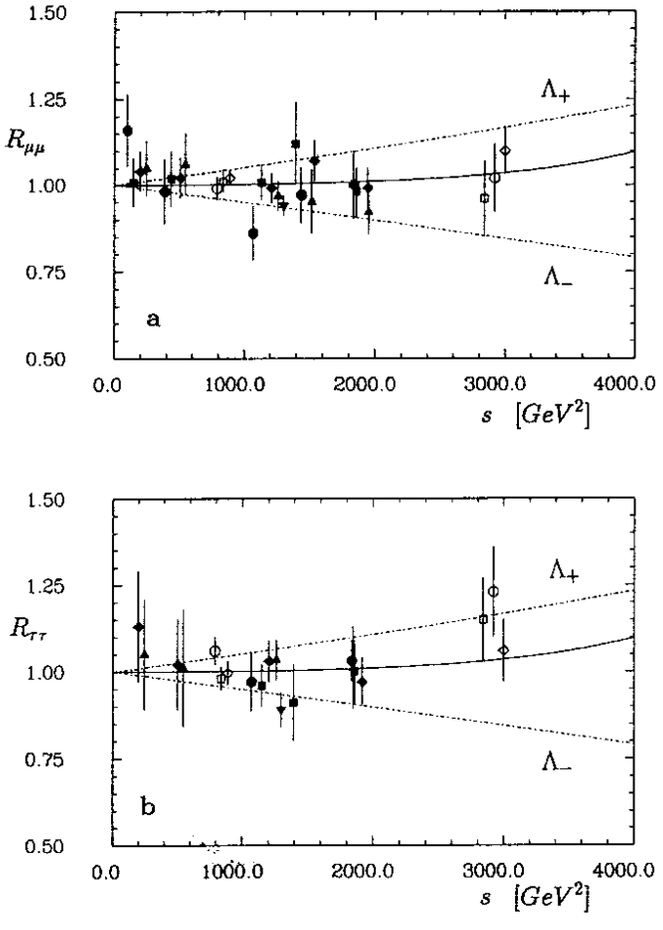


Figure 23: Total cross sections normalized to QED as a function of the centre of mass energy squared $s$. a) $R_{\mu\mu}$ for $e^+e^- \to \mu^+\mu^-$, b) $R_{\tau\tau}$ for $e^+e^- \to \tau^+\tau^-$. Data are from PETRA (full symbols), PEP (open symbols) and TRISTAN (open symbols) experiments and contain systematic uncertainties. The full curves show the QFD expectation. The dashed curves show the deviation from QED for cut-off parameters $\Lambda = 200\,GeV$



form factor, which modifies the total cross section according to

$$\sigma(e^+e^- \to l^+l^-) = \frac{4\pi\alpha^2}{3s}\left(1 \mp \frac{s}{s-\Lambda_\pm^2}\right)^2 . \qquad (48)$$

After correcting for the small electroweak effects (assuming the validity of the standard theory with $\sin^2\theta_W = 0.23$ and $m_Z = 92\,GeV$), fits to the data yield lower limits on the QED cut-off parameters for the reactions $e^+e^- \to \mu^+\mu^-$ and $e^+e^- \to \tau^+\tau^-$ summarized in Table 5. They reach values above 250 GeV. The effect of a cut-off parameter of $\Lambda = 200\,GeV$ on the total cross section measurements is illustrated in Figs. 23. At very high energies such an interpretation of the data certainly becomes doubtful and should instead be compared to the QFD predictions.

Table 5: Lower limits (95 % confidence level) on QED cut-off parameters for the reactions $e^+e^- \to \mu^+\mu^-$ and $e^+e^- \to \tau^+\tau^-$

| | $e^+e^- \to \mu^+\mu^-$ | | $e^+e^- \to \tau^+\tau^-$ | |
|---|---|---|---|---|
| Experiment | $\Lambda_+$ $[GeV]$ | $\Lambda_-$ $[GeV]$ | $\Lambda_+$ $[GeV]$ | $\Lambda_-$ $[GeV]$ |
| HRS [40,41] | 170 | 146 | 92 | 246 |
| MAC [42] | 172 | 172 | — | — |
| CELLO [43,44] | 230 | 171 | 142 | 121 |
| JADE [35] | 230 | 245 | 285 | 210 |
| MARK J [36,45] | 355 | 209 | 235 | 205 |
| PLUTO [37,46] | 206 | 141 | 79 | 63 |
| TASSO [47,48] | 325 | 150 | 184 | 221 |
| AMY [29] | 265 | 220 | — | — |
| TOPAZ [39] | 330 | 128 | — | — |
| VENUS [39] | 188 | 265 | — | — |

**Summary on two particle final states.** The cleanest QED reaction $e^+e^- \to \gamma\gamma$ has been measured very precisely. The $\mathcal{O}(\alpha^3)$ differential cross section including virtual and bremsstrahlung radiative corrections is found to be in agreement with QED at the one percent level. QED cut-off parameters of $\Lambda_+ > 98\,GeV$ and $\Lambda_- > 80\,GeV$ exclude excited heavy electrons of this mass. The differential Bhabha cross section $e^+e^- \to e^+e^-$ confirms $\mathcal{O}(\alpha^3)$ QED calculations at the level of a few percent, but indicates the presence of electroweak effects. The total cross section measurements for the reactions $e^+e^- \to \mu^+\mu^-$ and $e^+e^- \to \tau^+\tau^-$ are well described by $\mathcal{O}(\alpha^3)$ QED within a few percent up to energies of 55 GeV. Lower limits on the lepton QED cut-off parameters $\Lambda$ exceed values of 250 GeV and suggest that the electron, the muon and the tau behave as pointlike particles down to distances smaller than $10^{-16}\,cm$. This is very remarkable, since the lepton masses differ by more than 3 orders of magnitude and the $\tau$ is about twice as heavy as the proton.

## 7.2 Hard photon radiation processes

In section 4 on radiative corrections it was pointed out that first order corrections to the basic two body processes can become quite large. It is therefore very important to test these calculations experimentally. Among the $\mathcal{O}(\alpha^3)$ QED corrections the initial and final state photon bremsstrahlung give the largest contributions. An example of collinear photon emission is the acollinearity angle distribution of $\mu$ pair production shown in Fig. 22. In this section experimental results on processes involving hard photon radiation will be presented.

Experimental studies have been performed for the $\mathcal{O}(\alpha^3)$ and $\mathcal{O}(\alpha^4)$ final states listed in Table 6. The signature is that one or two photons are scattered under a large polar angle inside the detector acceptance and are well separated from the other particles. The event samples consist of the order of hundred to thousand three particle final states and of the order of ten to hundred four particle final states for each experiment. Since the event selection criteria are very specific to each experiment, a comparison of data with QED can only be done with the help of detailed Monte Carlo simulations. For $e^+e^-$ annihilation into lepton pairs obviously the lowest order $Z^0$ exchange diagrams have to be included. Qualitative and quantitative comparisons with QED are provided through a number of characteristic distributions and by comparing absolute rates.

Fig. 24 shows the energy and polar angle distributions of the photons in the reaction $e^+e^- \to \gamma\gamma\gamma$ measured by JADE. While most of the photons have an energy around $E_\gamma/E_{beam} \simeq 1$ the spectrum rises towards low energies exhibiting the typical bremsstrahlung behaviour. One also observes that the angular distribution becomes flatter compared to the $e^+e^- \to \gamma\gamma$ reaction (Fig. 16a), because the additional photon is produced almost isotropically. The agreement of the three and four photon final state data with $\mathcal{O}(\alpha^3)$ and $\mathcal{O}(\alpha^4)$ QED simulations is generally good concerning the shapes of the distributions as well as the rates. Similar conclusions have been reached by MAC (see Table 6).

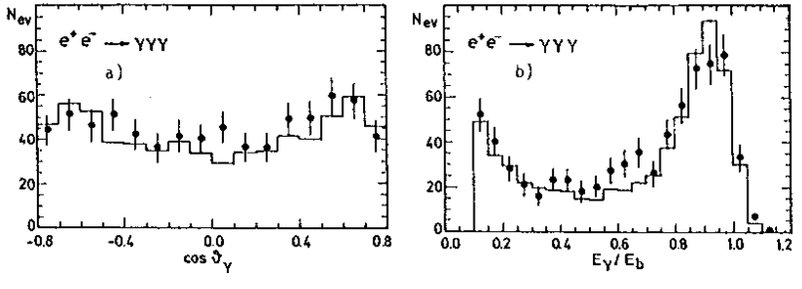


Figure 24: Distributions for the reaction $e^+e^- \to \gamma\gamma\gamma$ measured by JADE at $\sqrt{s} = 34.4\,GeV$ (3 entries/event). a) Polar angle $\theta_\gamma$, b) photon energy $E_\gamma/E_{beam}$. The histograms show the $\mathcal{O}(\alpha^3)$ QED predictions



Table 6: Data samples on photonic and leptonic $\mathcal{O}(\alpha^3)$ and $\mathcal{O}(\alpha^4)$ processes involving one or two additional photons in the final state and comparison with QED predictions

| Experiment | Final state | $\sqrt{<s>}$ $[GeV]$ | No. events observed | No. events predicted |
|---|---|---|---|---|
| JADE [49] | $\gamma\gamma\gamma$ | 34.4 | 246 | $235 \pm 4$ |
| | $\gamma\gamma\gamma\gamma$ | | 10 | $9.0 \pm 0.3$ |
| MAC [23] | $\gamma\gamma\gamma$ | 29 | 284 | 310.6 |
| CELLO [50] | $e^+e^-\gamma$ | 14 – 46.8 | 654 | 661.5 |
| JADE [49] | $e^+e^-\gamma$ | 34.4 | 3227 | $3320 \pm 9$ |
| | $e^+e^-\gamma\gamma$ | | 176 | $170 \pm 5$ |
| CELLO [50] | $\mu^+\mu^-\gamma$ | 14 – 46.8 | 62 | 59.8 |
| JADE [49] | $\mu^+\mu^-\gamma$ | 27 – 36.6 | 270 | 290 |
| | $\mu^+\mu^-\gamma\gamma$ | | 16 | 11.7 |
| MAC [51] | $\mu^+\mu^-\gamma$ | 29 | 273 | 280 |
| | $\mu^+\mu^-\gamma\gamma$ | | 17 | 14 |
| MARK J [52] | $\mu^+\mu^-\gamma$ | 28.7 – 46.0 | 795 | 811 |
| JADE [49] | $\tau^+\tau^-\gamma$ | 30 – 46.8 | 112 | $100 \pm 3$ |
| | $\tau^+\tau^-\gamma\gamma$ | | $9.4 \pm 3.3$ | 9.7 |

Fig. 25 shows photon and electron distributions for the reactions $e^+e^- \to e^+e^-\gamma$ and $e^+e^- \to e^+e^-\gamma\gamma$ measured by JADE. The photon energy spectra show the typical bremsstrahlung nature. They peak at low values but have long tails extending up to the maximum energy of $E_\gamma/E_{beam} \simeq 1$. The photon angular distribution in the reaction $e^+e^- \to e^+e^-\gamma\gamma$ becomes relatively flat except for angles close to the $e^\pm$ beams. The photons are emitted almost isotropically in the central detector region. The interference of the initial and final state bremsstrahlung diagrams leads to a negative forward backward asymmetry in the lepton polar angle distribution (see section 4). This effect is very large in the reaction $e^+e^- \to e^+e^-\gamma$ (Fig. 25b). The forward region is drastically depopulated compared to the pure Bhabha scattering (Figs. 19 and 20a). Similar investigations have been done by CELLO. The agreement between the data and $\mathcal{O}(\alpha^3)$ and $\mathcal{O}(\alpha^4)$ QED simulations is in all cases satisfactory at the level of a few percent (see Table 6).

The reactions $e^+e^- \to \mu^+\mu^-\gamma$ and $e^+e^- \to \mu^+\mu^-\gamma\gamma$ have been studied by several experiments. Fig. 26 shows some distributions for the reactions $e^+e^- \to \mu^+\mu^-\gamma$ and $e^+e^- \to \mu^+\mu^-\gamma\gamma$ from the MAC experiment. The $\mu\gamma$ invariant mass distributions are well described by phase space and give no hints for an excited muon decaying into a muon and a photon. The CELLO collaboration reported a two standard deviation excess of events in the reaction $e^+e^- \to \mu^+\mu^-\gamma$ at high invariant mass $m^2_{\mu\gamma}/s > 0.8$ for

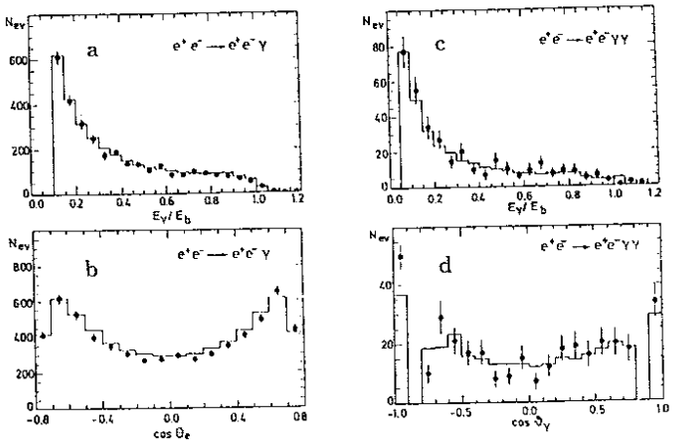


Figure 25: Distributions for the reactions $e^+e^- \to e^+e^-\gamma$ and $e^+e^- \to e^+e^-\gamma\gamma$ measured by JADE at $\sqrt{s} = 34.4\,GeV$. $e^+e^- \to e^+e^-\gamma$: a) photon energy $E_\gamma/E_{beam}$, b) electron polar angle $\theta_e$ (2 entries/event); $e^+e^- \to e^+e^-\gamma\gamma$ (2 entries/event): c) photon energy $E_\gamma/E_{beam}$, d) photon polar angle $\theta_\gamma$. The histograms show the $\mathcal{O}(\alpha^3)$ and $\mathcal{O}(\alpha^4)$ QED predictions

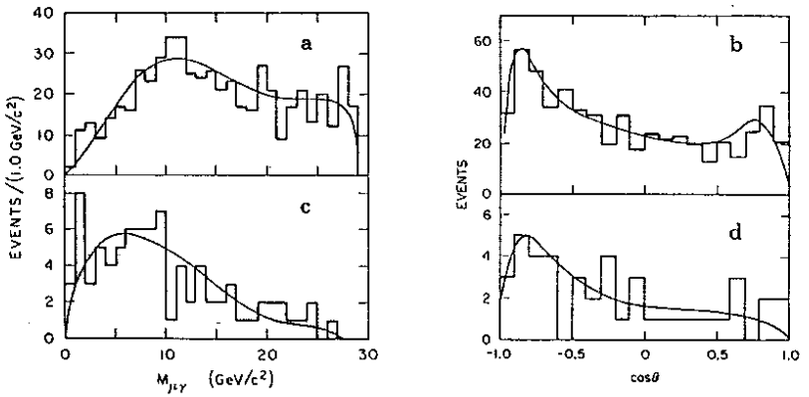


Figure 26: Distributions for the reactions $e^+e^- \to \mu^+\mu^-\gamma$ and $e^+e^- \to \mu^+\mu^-\gamma\gamma$ measured by MAC at $\sqrt{s} = 29\,GeV$. $e^+e^- \to \mu^+\mu^-\gamma$: a) $\mu\gamma$ invariant mass (2 entries/event), b) $\mu$ polar angle $\theta_\mu$; $e^+e^- \to \mu^+\mu^-\gamma\gamma$: c) $\mu\gamma$ invariant mass (4 entries/event), b) $\mu$ polar angle $\theta_\mu$. The curves show the $\mathcal{O}(\alpha^3)$ and $\mathcal{O}(\alpha^4)$ QED predictions



centre of mass energies above 34 GeV. This observation was, however, not confirmed by other experiments [49,53]. The muon polar angle distributions (Figs. 26b,d) exhibit large negative forward backward asymmetries caused by the interference of the initial and final state bremsstrahlung diagrams. The results on the asymmetry in the reaction $e^+e^- \to \mu^+\mu^-\gamma$ obtained by MAC, MARK J and JADE are summarized in Table 7. They are in good agreement with QED as well as with QFD. Note that the major part of the asymmetry is due to QED and that its value is very large and negative. This has to be compared with the positive QED induced asymmetry of about +2% in the analysis of $e^+e^- \to \mu^+\mu^-$ requiring an acollinearity angle of $\xi < 10^0$ (see section 4). The bremsstrahlung contributions can be varied by choosing different photon energy cuts. JADE and MARK J found that the absolute magnitude of the asymmetry decreases with rising photon energy cut in accordance with QED. The distributions and rates for both reactions $e^+e^- \to \mu^+\mu^-\gamma$ and $e^+e^- \to \mu^+\mu^-\gamma\gamma$ are in good agreement with $\mathcal{O}(\alpha^3)$ and $\mathcal{O}(\alpha^4)$ QED calculations.

Table 7: Charge asymmetries in the reactions $e^+e^- \to \mu^+\mu^-\gamma$ and $e^+e^- \to \tau^+\tau^-\gamma$ compared with QED and QFD predictions

| Experiment | Final state | $\sqrt{s}$ | $A^{meas}$ [%] | $A^{QED}$ [%] | $A^{QFD}$ [%] |
|---|---|---|---|---|---|
| JADE [49] | $\mu^+\mu^-\gamma$ | 27 – 36.6 | $-39 \pm 8$ | $-34 \pm 1$ | $-40 \pm 1$ |
| MAC [51] | $\mu^+\mu^-\gamma$ | 29 | $-21.6 \pm 4.1$ | $-21.1 \pm 1.3$ | |
| MARK J [52] | $\mu^+\mu^-\gamma$ | 28.7 – 46.0 | $-14.7 \pm 3.6$ | $-11.6 \pm 1.3$ | $-18.4 \pm 1.3$ |
| JADE [49] | $\tau^+\tau^-\gamma$ | 30 – 46.8 | $-27.6 \pm 8.7$ | $-31.4 \pm 2.2$ | $-36.2 \pm 4$ |

The reactions $e^+e^- \to \tau^+\tau^-\gamma$ and $e^+e^- \to \tau^+\tau^-\gamma\gamma$ are experimentally more difficult to access, since photons from $\tau$ decays have to be efficiently removed. Photon energy and $\tau$ angular distributions of the reaction $e^+e^- \to \tau^+\tau^-\gamma$ measured by JADE are presented in Fig. 27 . Again the photon bremsstrahlung spectrum is well described by QED. This also holds for the $\tau$ angular distribution, which shows a large negative forward backward asymmetry. The result on the asymmetry is given in Table 7, it is consistent with QED as well as with the standard theory. The data of both reactions $e^+e^- \to \tau^+\tau^-\gamma$ and $e^+e^- \to \tau^+\tau^-\gamma\gamma$ are in good agreement with the QED predictions (see Table 6).

**Summary on hard photon radiation processes.** Radiative processes with one or two additional hard photons have been studied in great detail. Characteristic distributions as well as absolute rates are in good agreement with $\mathcal{O}(\alpha^3)$ and $\mathcal{O}(\alpha^4)$ QED calculations at the level of 5 – 10 %. The available Monte Carlo event generators are able to reproduce the experimental data in almost all kinematical regions with sufficient accuracy. Finally the quality of the QED tests allows to set lower limits on the production of excited heavy leptons decaying into a lepton and a photon.

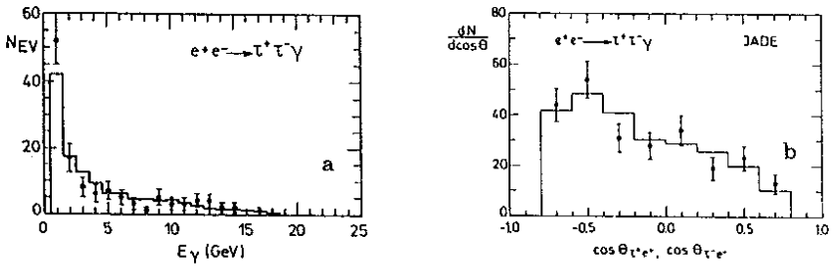


Figure 27: Distributions for the reaction $e^+e^- \to \tau^+\tau^-\gamma$ measured by JADE at $\sqrt{s} = 34.4\,GeV$. a) Photon energy $E_\gamma$, b) $\tau$ polar angle $\theta_\tau$. The histograms show the $\mathcal{O}(\alpha^3)$ QED predictions

## 7.3 Photon–photon collisions

Experimental QED tests in photon–photon collisions have been performed by studying the lepton pair production $e^+e^- \to e^+e^-e^+e^-$ and $e^+e^- \to e^+e^-\mu^+\mu^-$. Three types of $\mathcal{O}(\alpha^4)$ QED diagrams contribute to four lepton final states as sketched in Fig. 28. The dominant process is the photon–photon interaction or multiperipheral graph involving two space-like photons with $q^2_{\gamma 1} < 0$ and $q^2_{\gamma 2} < 0$. In addition there occur single conversions with one space-like and one time-like photon, $q^2_{\gamma 1} < 0$ and $q^2_{\gamma 2} > 0$, and double conversions with two time-like photons, $q^2_{\gamma 1} > 0$ and $q^2_{\gamma 2} > 0$. The latter two contributions are small, of the order of a few percent compared to the multiperipheral graph, and can, in principle, be disentangled by searching for low mass di-lepton pairs.

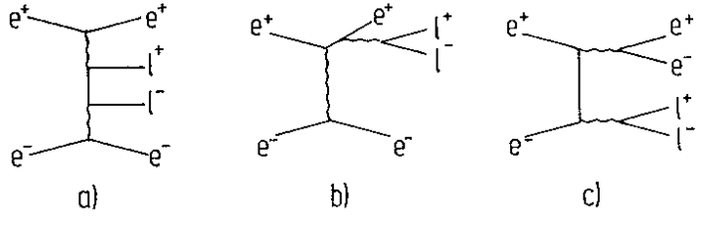


Figure 28: Feynman graphs contributing to the reaction $e^+e^- \to e^+e^-l^+l^-$. a) Photon–photon collision or multiperipheral process, b) single photon conversion, c) double photon conversion

As discussed in section 5 photon–photon collisions can be subdivided into the following classes: (i) no-tag events where both photons are quasi real and the electron/positron remains almost undeflected in the beam pipe, (ii) single-tag events



where one photon is highly virtual and the electron/positron is scattered into the detector, (iii) double-tag events where both photons are highly virtual and both the electron and the positron are detected in the apparatus. The electron/positron tagging is usually done with shower counters in the very forward or backward regions or in the central detector, where the rate decreases considerably with increasing scattering angle. The available data samples on photon–photon experiments are compiled in Table 8 together with the experimental conditions and a comparison with the QED predictions. The kinematical quantitites are defined in section 5. The accessible momentum transfers are quite low compared to the annihilation processes. Therefore it is not very meaningful to analyze the data in terms of QED cut-off parameters, which cannot compete with those derived in $e^+e^-$ annihilation events.

Table 8: Data samples of photon–photon collision experiments for the reactions $e^+e^- \to e^+e^-l^+l^-$ and comparison with QED predictions

| Experiment | $\sqrt{s}$ [ $GeV$ ] | $Q^2$ [ $GeV^2$ ] | Observed particles | Tag | Events observed | Events predicted |
|---|---|---|---|---|---|---|
| MAC [54] | 29 | $\simeq 0$ | $\mu\mu$ | no | $4849 \pm 122$ | $5090 \pm 260$ |
| PEP-9 [55] | 29 | $< 1.7$ | $e\mu\mu$ | single | 3400 | |
| CELLO [56] | 35 - 46.8 | 0.5 - 800 | $eee$ | single | 3358 | $3330 \pm 113$ |
| | | | $e\mu\mu$ | single | 1415 | $1387 \pm 56$ |
| | | | $eeee$ | double | 45 | 48 |
| | | | $ee\mu\mu$ | double | 28 | 30 |
| JADE [57] | 29 - 46.8 | 9 - 1200 | $eeee$ | double | 13 | $12.0 \pm 0.6$ |
| | | | $ee\mu\mu$ | double | 8 | $8.6 \pm 0.5$ |
| MARK J [52] | 30 - 46.8 | 0.7 - 166 | $\mu\mu$ | no | $3671 \pm 61$ | $3834 \pm 31$ |
| | | | $e\mu\mu$ | single | $283 \pm 17$ | $256 \pm 8$ |
| | | | $ee\mu, ee\mu\mu$ | double | $43 \pm 7$ | $39 \pm 3$ |
| PLUTO [58] | 35 | 0.1 - 100 | $e\mu\mu$ | single | $643 \pm 40$ | $674 \pm 32$ |

Studies of the process $e^+e^- \to e^+e^-\mu^+\mu^-$ with untagged electrons/positrons have been presented by MAC and MARK J. Data on the reaction $e^+e^- \to e^+e^-e^+e^-$ in the no-tag mode do not exist, because they are very difficult to discriminate against the high background from radiative Bhabha scattering events $e^+e^- \to e^+e^-\gamma$. Muon pairs from two-photon events can easily be separated from one-photon annihilation due to their low momenta. Furthermore transverse momentum balance requires that the two tracks are coplanar, i.e. appear to be back-to-back in the plane perpendicular to the $e^\pm$ beam direction, while the moving centre of mass system causes an almost flat acollinearity angle distribution. The invariant di-muon mass distribution is shown in Fig. 29a for the MARK J data taken at $\sqrt{s} = 44\,GeV$. One notices the rapidly falling spectrum towards high masses. The low mass part is affected by detector acceptance. There is no indication of a state with charge conjugation $C = +1$ decaying into a $\mu^+\mu^-$ pair. The data are well described by the QED Monte Carlo simulation.

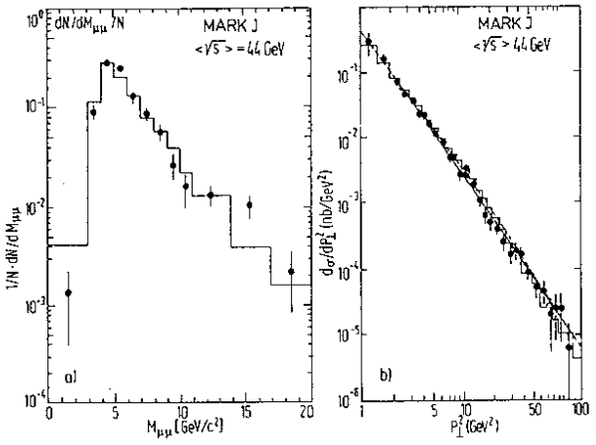


Figure 29: Distributions for the reaction $e^+e^- \to e^+e^-\mu^+\mu^-$ from MARK J at $\sqrt{s} = 44\,GeV$. a) The observed invariant di-muon mass $M_{\mu\mu}$, b) the differential cross section as a function of the muon transverse momentum squared $p_\perp^2$. The histograms show the $\mathcal{O}(\alpha^4)$ QED predictions. The broken line shows the Weizsäcker-Williams approximation and the full line a fit to the $p_\perp^2$ distribution

Fig. 29b shows the differential cross section as a function of the transverse momentum squared $d\sigma/dp_\perp^2$, where $p_\perp$ is measured with respect to the $e^\pm$ beam direction. Also shown is the $\mathcal{O}(\alpha^4)$ QED prediction. Both the exact formula and the Weizsäcker–Williams approximation describe the data equally well. The differential cross section can be well fitted by a power law behaviour

$$d\sigma/dp_\perp^2 = A \cdot p_\perp^n$$

with $n = 4.47 \pm 0.15$. For peripheral processes with massless particles and infinite centre of mass energy one expects [17] the exponent to be $n = 4$, close to the observed value. The MAC collaboration has performed a similar analysis and obtained with a slightly different parametrization $n = (4.00 \pm 0.12) + (0.019 \pm 0.004)\,p_\perp^2$ for the $p_\perp^2$ range of $3 - 30\,GeV^2/c^2$. It is interesting to note that $n$ approaches the theoretical value of 4 as $p_\perp^2 \to 0$. To substantiate this hypothesis will require much more data.

The total cross section for the reaction $e^+e^- \to e^+e^-\mu^+\mu^-$ as a function of the $e^+e^-$ centre of mass energy is displayed in Fig. 30 as measured by MARK J. The cross section of the untagged data rises logarithmically with the energy and becomes even larger than the annihilation cross section as expected. The measurements exhibit a remarkable agreement with the $\mathcal{O}(\alpha^4)$ QED predictions.

Tagged photon–photon collisions have been studied in both reactions $e^+e^- \to e^+e^-e^+e^-$ and $e^+e^- \to e^+e^-\mu^+\mu^-$. Through a measurement of the scattered electron/positron energy and direction the squared momentum transfer $Q^2$ can be deter-



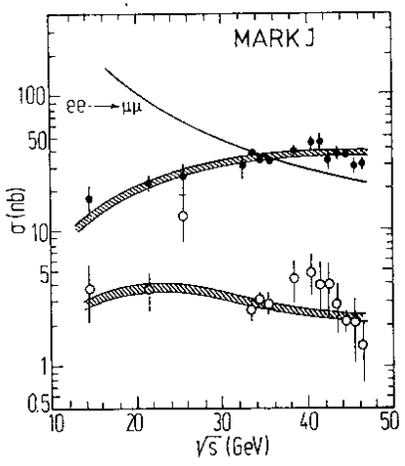


Figure 30: The total cross section for the reaction $e^+e^- \to e^+e^-\mu^+\mu^-$ from MARK J as a function of the $e^+e^-$ centre of mass energy. The dots represent the untagged data, the circles the tagged data. The curves show the $\mathcal{O}(\alpha^4)$ QED predictions and the $e^+e^- \to \mu^+\mu^-$ cross section for comparison

mined. The experiments prefer to show distributions of various kinematic quanitites like $Q^2$, W, $x$, momenta, invariant masses, etc., for limited $Q^2$ regions as given by the geometrical postion and acceptance of the tagging devices. In general the distributions agree well with $\mathcal{O}(\alpha^4)$ QED simulations concerning the shape as well as the absolute rate. Fig. 30 shows the total cross section for tagged two-photon muon pair production as a function of the $e^+e^-$ centre of mass energy measured by MARK J. The observed cross sections are about an order of magnitude lower than those of the tagged data and are well described by the QED predictions.

Of particular interest is the deep inelastic scattering of electrons off an almost real photon target. This process is described by two structure functions, eq.(42), of which under usual experimental conditions only one, namely $F_2(x, Q^2)$ is accessible.

The PEP-9/$\gamma\gamma$ collaboration has made a careful study of the reaction $e\gamma \to e\mu^+\mu^-$ at $\sqrt{s} = 29\,GeV$. The electron/positron is tagged at angles between 30 and 90 mrad, thus covering a momentum transfer range of $0 < Q^2 < 1.7\,GeV^2$. Fig. 31 shows differential cross sections as function of the muon scattering angle $\theta_\mu^*$ (measured in the $\mu^+\mu^-$ centre of mass system) and of the scaling variable $x$. One clearly observes a peaking of $\theta_\mu^*$ along the virtual photon directions which coincide with the $e^\pm$ beams. Both distributions agree well with the QED Monte Carlo simulation including all diagrams of Fig. 28. After integration over $\cos\theta_\mu^*$ the formula (42) can be applied. A further cut on the relative energy transfer $y < 0.25$ suppresses contributions from $F_1$ and allows to use the approximation of eq.(43) for $F_2(x, Q^2)$. The structure function $F_2(x)$, i.e. $F_2(x, Q^2)$ averaged over $Q^2$, is extracted by comparing the data to a Monte

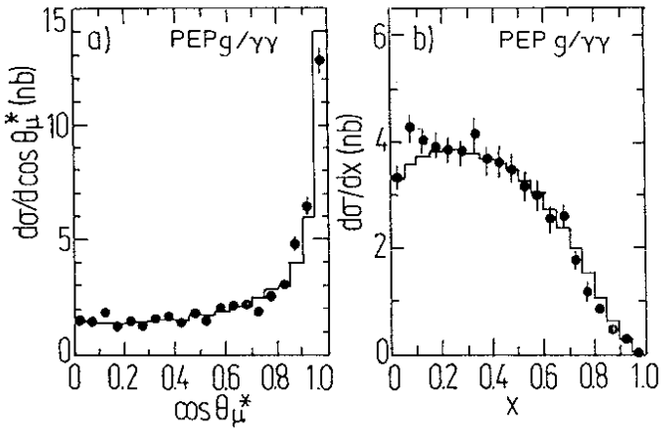


Figure 31: Differential cross section distributions for single tag $e^+e^- \to e^+e^-\mu^+\mu^-$ events from PEP-9/$\gamma\gamma$ at $\sqrt{s} = 29\,GeV$. a) $d\sigma/d\cos\theta^*_\mu$, b) $d\sigma/dx$. The histograms show the $\mathcal{O}(\alpha^4)$ QED simulations

Carlo event sample generated with $F_2 = 1$ and $F_1 = 0$. The result is shown in Fig. 32. One observes that $F_2(x)$ rises and remains large with increasing $x$ values, characteristic for a poinlike interaction. The acceptance corrected data can be directly compared to the QED predictions taken at average values of $Q^2 \simeq 0.5\,GeV^2$. It is interesting to note that the structure function $F_2$ is very sensitive to the muon mass and would allow a mass determination within about 10%. It is essentially this mass dependence which makes the photon structure function $F_2$ attractive for a determination of the QCD mass scale parameter $\Lambda_{QCD}$ in two–photn hadron production (see [59] and Kolanoski and Zerwas [18]). These results are a very beautiful confirmation of the $\mathcal{O}(\alpha^4)$ QED calculations in photon–photon collisions.

The CELLO collaboration has carried out an analysis of four lepton final states in the double tagged reactions $e^+e^- \to e^+e^-e^+e^-$ and $e^+e^- \to e^+e^-\mu^+\mu^-$ over a large $Q^2$ range. The data can be well described by QED once all graphs of Fig. 28 are included in the Monte Carlo simulation. The complete matrix element can be written as $\mathcal{M}(eell) = \alpha_0\mathcal{M}_0 + \alpha_1\mathcal{M}_1 + \alpha_2\mathcal{M}_2$, where the indices 0, 1 and 2 denote the multiperipheral, single conversion and double conversion contributions, respectively. The conversion diagrams essentially contribute to high the $x$ values covered by this experiment. From a simultaneous fit to all data they find for the coefficients $\alpha_0 = +0.94 \pm 0.08$, $\alpha_1 = +1.02 \pm 0.08$ and $\alpha_2 = +1.05 \pm 0.30$ in agreement with the expectation. The relative signs occur through interferences of the different graphs. This result provides clear evidence for the (although small) non–multiperipheral contributions and again support the $\mathcal{O}(\alpha^4)$ QED calculations.

To summarize lepton pair production in untagged and tagged photon–photon collisions is found to be in good agreement with QED and confirm the $\mathcal{O}(\alpha^4)$ cal-



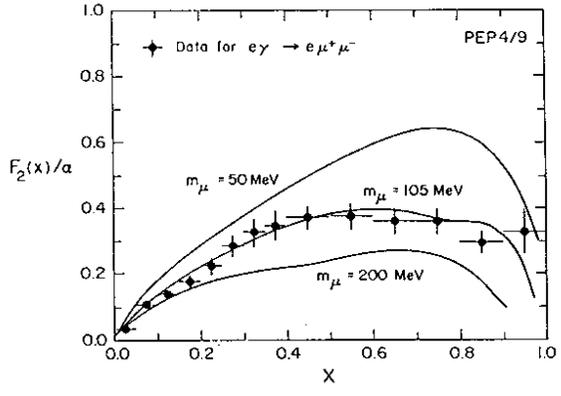


Figure 32: The structure function $F_2(x)$ for the reaction $e^+e^- \to e^+e^-\mu^+\mu^-$ from PEP-9/$\gamma\gamma$ at $\sqrt{s} = 29\,GeV$. The curves show the sensitivity to different values of the muon mass

culations at the level of ten percent. The 'muonic' photon structure function $F_2(x)$ demonstrates the pointlike interaction of the photon with the muon pair and is very sensitive to the muon mass.

# 8 Experimental tests of QFD

A review on experimental tests of the validity of QED in high energy electron–positron collisons would be incomplete without mentioning its 'natural' break down due to the weak interaction. Meanwhile the gauge invariant electroweak standard theory or QFD, unifying QED and the weak interaction, has been theoretically and experimentally well established. At the PETRA, PEP and TRISTAN $e^+e^-$ colliders the electroweak interaction manifests itself in $\gamma - Z^0$ interference phenomena leading to appreciable asymmetries in fermion pair production as well as in the rise of the normalized total hadronic cross section at centre of mass energies above $\sqrt{s} \simeq 35\,GeV$ due to the tail of the $Z^0$ resonance.

In the following section lepton and quark angular asymmetries and the total hadronic cross section will be discussed briefly with emphasis on the determination of the electroweak parameters of the standard theory. More detailed information can be found in [18], a collection of articles on $e^+e^-$ physics published in the same series as this volume, or in the recent compilation of electroweak interactions by [1].

## 8.1 Lepton asymmetries

The differential cross section distributions of Bhabha scattering $e^+e^- \to e^+e^-$ are shown in Fig. 21. The electroweak interference effects are very small and often comparable to the achieved experimental precision. Therefore the significance of individual experiments is generally poor. In Fig. 33 the results of a two parameter fit to the vector and axial vector couplings obtained by HRS and MAC are shown in the $g_V^{e\,2} - g_A^{e\,2}$ plane. The two parameters are highly correlated (correlation coefficient of 0.5 to 1) and depend sensitively on the absolute normalization. Both experiments claim to exclude pure QED at the level of 2 standard deviations. Results on $g_V^{e\,2}$ and $g_A^{e\,2}$ are summarized in Table 9. The individual experiments are certainly consistent

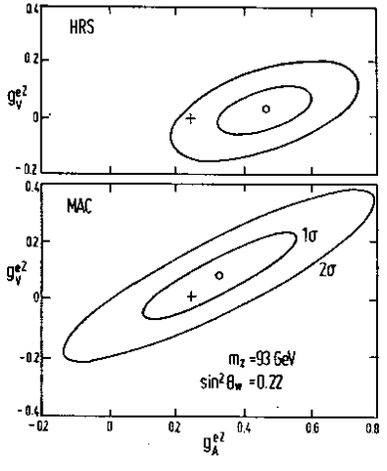


Figure 33: Correlation of vector coupling versus axial vector coupling constants for the reaction $e^+e^- \to e^+e^-$. a) HRS at $\sqrt{s} = 29\,GeV$, b) MAC at $\sqrt{s} = 29\,GeV$. The QFD prediction is marked by the crosses

Table 9: Results on $g_V^{e\,2}$ and $g_A^{e\,2}$ from the reaction $e^+e^- \to e^+e^-$

| Experiment | $g_V^{e\,2}$ | $g_A^{e\,2}$ |
|---|---|---|
| HRS [32] | $0.03 \pm 0.09$ | $0.46 \pm 0.14$ |
| MAC [33] | $0.09 \pm 0.14$ | $0.33 \pm 0.24$ |
| JADE [60] | $0.02 \pm 0.10$ | $0.22 \pm 0.17$ |
| PLUTO [61] | $0.09 \pm 0.12$ | $0.39 \pm 0.20$ |
| TASSO [38] | $-0.08 \pm 0.04$ | $0.14 \pm 0.12$ |
| Average | $-0.035 \pm 0.032$ | $0.285 \pm 0.071$ |
| Standard theory | 0.002 | 0.25 |



with QFD. The average values do not take the correlations into account, which were not always published. They are in good agreement with the standard theory.

The weak mixing angle $\sin^2\theta_W$ cannot unambiguously be extracted from Bhabha scattering. The small value of $g_V^{e\,2} = (-1/2 + 2\sin^2\theta_W)^2$ implies a value of $\sin^2\theta_W$ close to 1/4 with a twofold ambiguity, which could only be resolved with a considerably improved precision. Consequently low cross section measurements resulting in negative values of $g_V^{e\,2}$ lead to unrealistically small errors on $\sin^2\theta_W$.

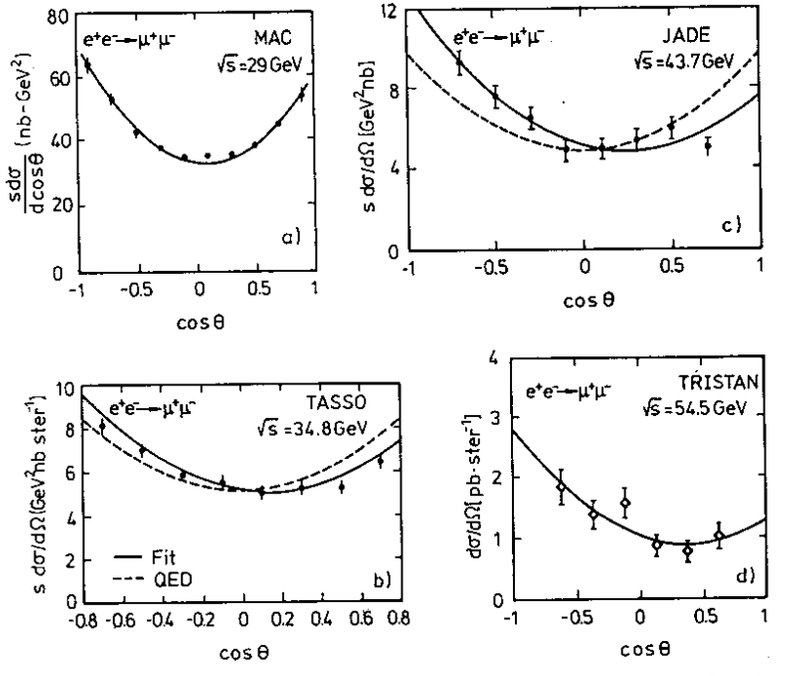


Figure 34: Differential cross sections for the reaction $e^+e^- \to \mu^+\mu^-$. a) MAC at $\sqrt{s} = 29\,GeV$, b) TASSO at $\sqrt{s} = 34.8\,GeV$, c) JADE at $\sqrt{s} = 43.7\,GeV$, d) combined TRISTAN experiments at $\sqrt{s} = 54.5\,GeV$

The reaction $e^+e^- \to \mu^+\mu^-$ was the first process where electroweak $\gamma - Z^0$ interference was observed at $e^+e^-$ colliders. QFD predicts a sizeable negative charge asymmetry in the differential cross section distribution at high energy (see Fig. 4). The first significant evidence on a forward backward charge asymmetry in the angular distributions was announced by PETRA experiments in 1981 [62]. Since then extensive measurements have been performed at PETRA, PEP and TRISTAN. Present experimental data are not sufficient to detect electroweak effects in the total lepton pair production cross section (see section 7).

Fig. 34 shows the differential cross section distributions for the reaction $e^+e^- \to \mu^+\mu^-$ measured by MAC, TASSO, JADE and TRISTAN experiments. All experiments measure a clear deviation from QED with a statistical significance of several standard deviations. The experimental results of the observed charge asymmetries $A_{\mu\mu}$ are plotted in Fig. 35 as a function of the centre of mass energy squared $s$. One notices a clear rise in absolute magnitude roughly proportional to $s$ in good agreement with the standard theory.

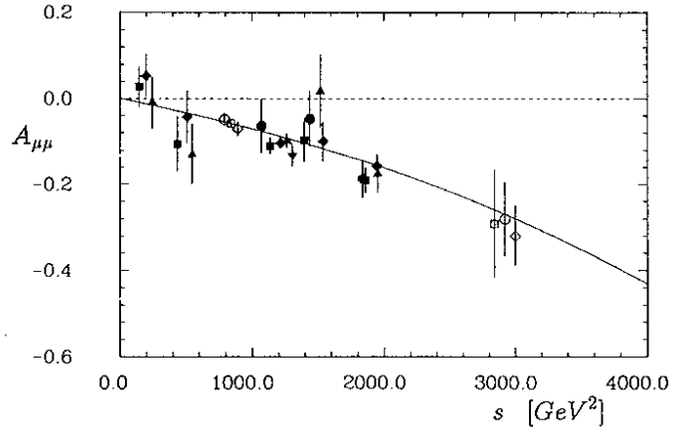


Figure 35: Measurements of the forward backward asymmetry $A_{\mu\mu}$ in the reaction $e^+e^- \to \mu^+\mu^-$ as a function of the centre of mass energy squared $s$. The curve shows the standard theory expectation for $\sin^2\theta_W = 0.23$ and $m_Z = 91.9\,GeV$

Since the asymmetry is a firm prediction of QFD, another way to compare the different experiments independent of the centre of mass energy is to extract the electroweak coupling constants. The charge asymmetry depends essentially on the axial vector couplings, while the total cross section depends essentially on the vector coupling constants. Both measurements can be used to determine the products of $g_A^e\, g_A^\mu$ and $g_V^e\, g_V^\mu$ with almost no correlation. The results are summarized in Table 10 together with average values. The data do not provide a precise measurement of the vector couplings, they rather put strong constraints on them. The axial vector couplings, however, deviate significantly from zero. The measured values are in very good agreement with the electroweak theory within one standard deviation or to better than 6%.

In the reaction $e^+e^- \to \tau^+\tau^-$ the same electroweak $\gamma - Z^0$ interference effects are expected as in $\mu$ pair production, since in QFD all charged leptons have identical vector and axial vector couplings and the mass of the $\tau$ is negligible. The data samples are in general smaller and have larger systematic uncertainties because only few experiments analyze all accessible $\tau$ decay modes.

Differential cross section measurements for the reaction $e^+e^- \to \tau^+\tau^-$ are shown



Table 10: Results on $g_V^e\, g_V^\mu$ and $g_A^e\, g_A^\mu$ from the reaction $e^+e^- \to \mu^+\mu^-$

| Experiment | $g_V^e\, g_V^\mu$ | $g_A^e\, g_A^\mu$ |
|---|---|---|
| HRS [40] | $0.03 \pm 0.10$ | $0.208 \pm 0.067$ |
| MAC [63] | $-0.02 \pm 0.09$ | $0.25 \pm 0.03$ |
| MARK II [64] | — | $0.32 \pm 0.07$ |
| CELLO [65] | — | $0.28 \pm 0.08$ |
| JADE [35] | $0.01 \pm 0.08$ | $0.325 \pm 0.043$ |
| MARK J [52] | $0.04 \pm 0.04$ | $0.280 \pm 0.035$ |
| PLUTO [66] | — | $0.35 \pm 0.08$ |
| TASSO [47] | $0.09 \pm 0.06$ | $0.264 \pm 0.037$ |
| AMY [67] | $0.01 \pm 0.08$ | $0.26 \pm 0.08$ |
| TOPAZ [67] | $0.07 \pm 0.10$ | $0.28 \pm 0.12$ |
| VENUS [67] | $-0.05 \pm 0.06$ | $0.29 \pm 0.06$ |
| Average | $0.025 \pm 0.022$ | $0.276 \pm 0.015$ |
| Standard theory | 0.002 | 0.25 |

Table 11: Results on $g_V^e\, g_V^\tau$ and $g_A^e\, g_A^\tau$ from the reaction $e^+e^- \to \tau^+\tau^-$

| Experiment | $g_V^e\, g_V^\tau$ | $g_A^e\, g_A^\tau$ |
|---|---|---|
| HRS [41] | — | $0.28 \pm 0.11$ |
| MAC [68] | $0.06 \pm 0.10$ | $0.24 \pm 0.05$ |
| MARK II [64] | — | $0.19 \pm 0.09$ |
| CELLO [44] | — | $0.28 \pm 0.14$ |
| JADE [35] | $0.08 \pm 0.07$ | $0.185 \pm 0.055$ |
| MARK J [52] | $0.07 \pm 0.07$ | $0.223 \pm 0.064$ |
| TASSO [48] | $-0.05 \pm 0.10$ | $0.18 \pm 0.09$ |
| AMY [67] | $-0.15 \pm 0.12$ | $0.32 \pm 0.09$ |
| TOPAZ [67] | $-0.11 \pm 0.10$ | $0.19 \pm 0.13$ |
| VENUS [67] | $-0.03 \pm 0.07$ | $0.18 \pm 0.10$ |
| Average | $-0.003 \pm 0.029$ | $0.231 \pm 0.022$ |
| Standard theory | 0.002 | 0.25 |

in Fig. 36 at four different energies around 29 GeV, 35 GeV, 44 GeV and 55 GeV. They exhibit a significant deviation from the QED prediction and show a negative forward backward charge asymmetry growing in modulus with energy.

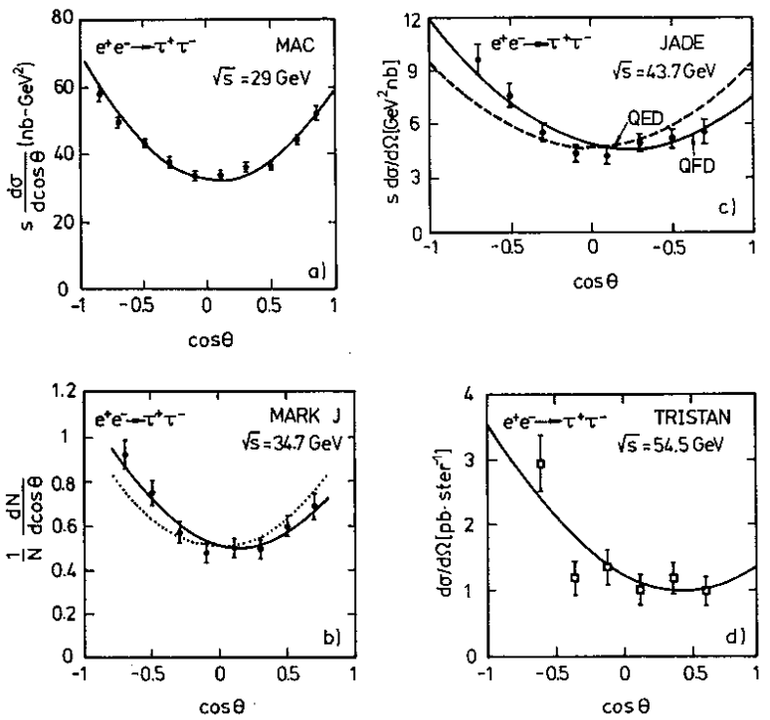


Figure 36: Differential cross sections for the reaction $e^+e^- \to \tau^+\tau^-$. a) MAC at $\sqrt{s} = 29\,GeV$, b) MARK J at $\sqrt{s} = 34.6\,GeV$, c) JADE at $\sqrt{s} = 43.7\,GeV$, d) combined TRISTAN experiments at $\sqrt{s} = 54.5\,GeV$

The measured asymmetries $A_{\tau\tau}$ from all experiments are displayed in Fig. 37 as a function of the centre of mass energy squared $s$. The values rise in absolute magnitude with $s$ and closely follow the QFD curve. The charge asymmetry in the reaction $e^+e^- \to \tau^+\tau^-$ is experimentally well established.

The results on the product of the vector couplings $g_V^e\, g_V^\tau$ and the axial vector couplings $g_A^e\, g_A^\tau$ are compiled in Table 11. Again they are in good agreement with QFD. The axial vector couplings of the $\tau$ and the $\mu$ differ by about 2 standard deviations, ${g_A^\tau}^2$ being lower and ${g_A^\mu}^2$ being higher than the standard theory prediction. This 'discrepancy' has been discussed for quite some time, regarding, e.g., whether



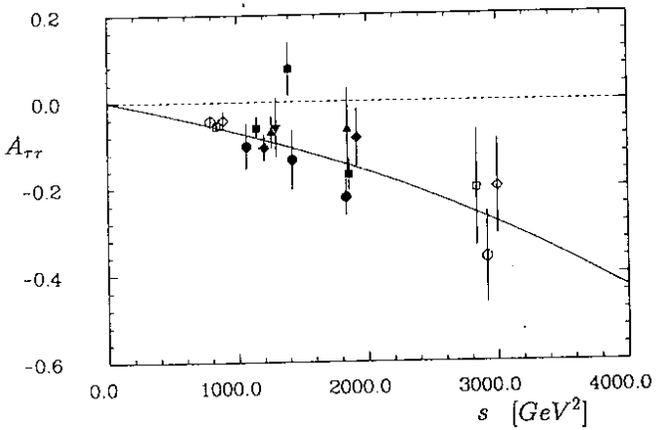


Figure 37: Measurements of the forward backward asymmetry $A_{\tau\tau}$ in the reaction $e^+e^- \to \tau^+\tau^-$ as a function of the centre of mass energy squared $s$. The curve shows the standard theory expectation for $\sin^2\theta_W = 0.23$ and $m_Z = 91.9\,GeV$

systematic effects in the more problematic $\tau$ analysis have not been correctly taken into account. No explanations other than statistical fluctuations have been found. Both reactions are certainly compatible with each other and confirm the standard theory prediction.

The electroweak couplings of the three leptonic reactions are in agreement with each other and support the concept of $e - \mu - \tau$ universality. It thus makes sense to assume lepton universality. A combined fit yields for the lepton coupling constants

$$ {g_V^l}^2 = 0.010 \pm 0.015\,, $$
$$ {g_A^l}^2 = 0.258 \pm 0.012\,. $$

In a single parameter fit one can determine the weak mixing angle $\sin^2\theta_W$. Using all data one finds for the leptonic sector in $e^+e^-$ experiments

$$ \sin^2\theta_W = 0.216 \pm 0.014\,. $$

This value is in agreement with the world average from all experiments and should in particular be compared to that obtained in low momentum transfer purely leptonic $\nu_\mu(\bar{\nu}_\mu)\, e \to \nu_\mu(\bar{\nu}_\mu)\, e$ scattering experiments [5], $\sin^2\theta_W = 0.223 \pm 0.018$.

## 8.2 Quark asymmetries

The electroweak standard theory predicts large asymmetries for quark pair production $e^+e^- \to q\bar{q} \to hadrons$ proportional to the inverse of the quark charge. Hadronic

annihilation events are experimentally readily separable from lepton final states and photon–photon collisions. The difficulty is to disentangle the individual quark flavours being produced proportional to their charge squared with comparable rates in the debris of hadrons. The heavy quarks $c$ and $b$ are essentially produced as primary quarks, while the light quarks are as well copiously produced in the fragmentation process and via hadron decays. Two methods have been developed to tag the heavy quark flavours: (i) the study of semileptonic decays with subsequent assignment of the original quark from the lepton charge; (ii) the reconstruction of the parent hadrons, in particular $D$ and $D^*$ mesons.

Prompt leptons from the heavy quarks $c$ and $b$ emerge in the following sequence (neglecting suppressed decay modes)

$$\begin{aligned} e^+e^- &\rightarrow c\bar{c} \\ &\hookrightarrow s\, l^+ \nu_l\,, \\ e^+e^- &\rightarrow b\bar{b} \\ &\hookrightarrow c\, l^- \bar{\nu}_l\,. \end{aligned}$$

The quark flavour is uniquely assigned to the lepton charge. (Here and in the following only states containing the heavy quark will be considered, charge conjugate states can be treated accordingly.) The analysis relies on two ingredients. Firstly, the heavy quarks are essentially produced as primary quarks with high fractional energy, thus they are aligned along the direction of the jet formed by the decay particles. Secondly, the quark masses are heavy, thus the decay leptons have high transverse momenta with respect to the quark or jet direction, up to half the quark mass. The light $u$, $d$, $s$ quarks decay semileptonically into low transverse momentum leptons with respect to the jet axis and can be easily separated. The charmed event sample has to be corrected for wrong sign leptons from $b$ quark decays. The observable bottom quark asymmetry will be reduced by a factor of about $1.25 \pm 0.1$ due to $B^0\bar{B}^0$ mixing [69].

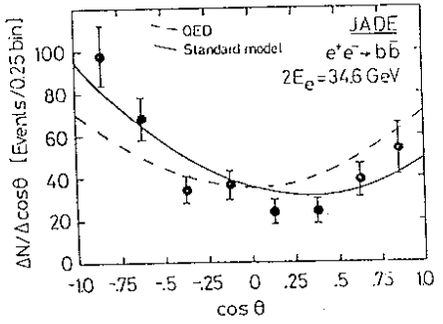


Figure 38: Angular distribution for the reaction $e^+e^- \rightarrow b\bar{b}$ using inclusive muons from JADE at $\sqrt{s} = 34.6\,GeV$. The full curve shows the QFD prediction, while the dashed curve shows the QED expectation

Several experiments on inclusive electron and muon spectra from heavy quark decays have been performed. Fig. 38 shows the $b$ quark angular distribution derived from inclusive muon spectra measured by JADE at $\sqrt{s} = 34.6\,GeV$, the most precise data. A distinct asymmetry of $A_{bb} = -22.8 \pm 6.5\,\%$ is seen in good agreement with



the QFD prediction of $A_{bb}^{QFD} = -25.6\,\%$ neglecting $B^0\bar{B}^0$ mixing. The asymmetry is about 3 times larger as for $\mu$ pairs at the same centre of mass energy, reflecting the charge $Q_b = -1/3$ of the $b$ quark.

A more direct method to tag heavy quarks is to reconstruct the parent mesons. At high energies this has so far only been accomplished for charmed mesons produced via the following chain

$$\begin{aligned} e^+e^- &\rightarrow c\bar{c} \\ &\hookrightarrow D^{*+}X \\ &\hookrightarrow D^0\pi^+ \\ &\hookrightarrow K^-\pi^+,\ K^-\pi^+\pi^0,\ K^-\pi^+\pi^+\pi^-,\ \ldots \end{aligned}$$

The experimental resolution is considerably improved by making use of the small mass difference $\Delta m = m_{D^{*+}} - m_{D^0}$, which can be measured much more accurately than the masses of the $D^{*+}$ or $D^0$ mesons themselves. The event samples are almost free of background, the main source being $b$ decays, but are statistically limited by the small branching ratios of low multiplicity hadronic $D$ meson decays. Fig. 39 shows the angular distribution of $D^*$ mesons measured by HRS at $\sqrt{s} = 29\,GeV$, which is the only experiment capable of identifying the decays $D^0 \rightarrow K^-\pi^+$ and $D^+ \rightarrow K^-\pi^+\pi^+$ directly without the above mentioned kinematical trick. The $D^*$ asymmetry is $-6.1 \pm 3.9\,\%$ to be compared with the QFD prediction of $-8.6\,\%$.

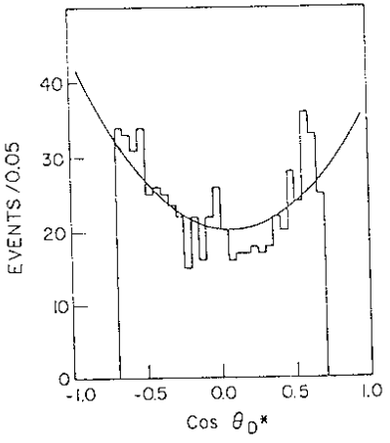


Figure 39: Angular distribution of $D^*$ mesons in the reaction $e^+e^- \rightarrow c\bar{c}$ from HRS at $\sqrt{s} = 29\,GeV$. The curve shows the measured asymmetry

Results on the axial vector couplings of the charm and bottom quarks deduced from the asymmetries of the most accurate experiments are compiled in Tables 12 and 13 (assuming $g_A^e = -1/2$ for the electron axial vector charge). The analysis methods are listed as well. With a few exceptions the signals of individual measurements are generally poor. The averaged values of the heavy quark axial vector couplings, however, have a significance of about 5 standard deviations and definitely support the standard theory predictions of $g_A^c = 1/2$ and $g_A^b = -1/2$. Note that the measured

Table 12: Results on the charm quark axial vector coupling $g_A^c$ from the reaction $e^+e^- \to c\bar{c}$

| Experiment | Method | $g_A^c$ |
|---|---|---|
| HRS [70] | $D^*$, $D$ | $0.58 \pm 0.16$ |
| TPC [71] | e, $\mu$, $D^*$ | $0.95 \pm 0.50$ |
| JADE [72] | $D^*$ | $0.55 \pm 0.25$ |
| MARK J [36] | $\mu$ | $0.60 \pm 0.30$ |
| TASSO [73] | $D^*$ | $0.55 \pm 0.15$ |
| Average | | $0.58 \pm 0.09$ |

Table 13: Results on the bottom quark axial vector coupling $g_A^b$ from the reaction $e^+e^- \to b\bar{b}$. The MARK II and JADE data are not corrected for $B^0\bar{B}^0$ mixing

| Experiment | Method | $g_A^b$ |
|---|---|---|
| MARK II [74] | e, $\mu$ | $-0.75 \pm 0.38$ |
| CELLO [75] | e, $\mu$ | $-0.60 \pm 0.22$ |
| JADE [76] | $\mu$ | $-0.45 \pm 0.13$ |
| TASSO [77] | e, $\mu$, jet charge | $-0.62 \pm 0.25$ |
| Average | | $-0.53 \pm 0.10$ |

axial vector coupling of the bottom quark requires that it is a member of a weak isospin doublet. This is the most significant argument that the still undiscovered top quark has to exist.

If no flavour tagging is possible, as e.g. for the light quarks, one can try to measure the elctroweak induced charge asymmetry of all quarks simultaneously. The asymmetries of the positively charged quarks and antiquarks tend to cancel each other and the residual asymmetry summed over 5 quarks is expected to have a very small value of

$$< A_q > \; = \; -\frac{3}{11} A_{\mu\mu} \, .$$

The charge of the primary leading quark should be reflected in the jet charge, which is the sum of all particle charges in a jet weighted with some function according to their momenta, favouring high momentum tracks. The axial vector couplings can then be deduced by a comparison with model calculations, but requires high statistics and excellent understanding of the detector as well as of the underlying hadronization model.



The first analysis of this type was carried out by MAC [78] at a centre of mass energy of $\sqrt{s} = 29\,GeV$. The jet angular distribution is shown in Fig. 40. The observed asymmetry is small but significant, which is best seen after subtracting the symmetric QED term and plotting the term linear in $\cos\theta$. The measured asymmetry is $A_{jet} = +2.8 \pm 0.5\,\%$ while the expected asymmetry including detector effects is $+2.0 \pm 0.5\,\%$. Similar analyses have been done subsequently by TASSO [79] and JADE [80] at 35 and 44 GeV.

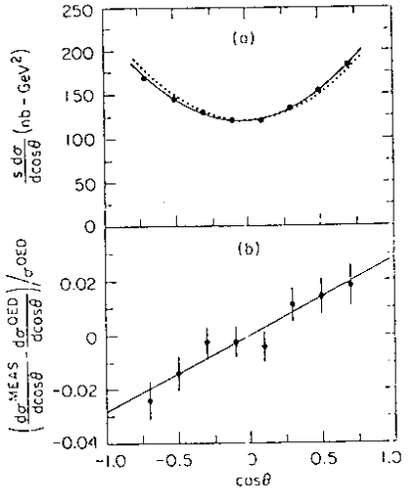


Figure 40: Jet angular distribution for the reaction $e^+e^- \to q\bar{q}$ from MAC at $\sqrt{s} = 29\,GeV$. The polar angle is measured between the positive jet and the $e^-$ direction. a) Differential cross section, b) difference between measurement and QED divided by QED. The full curves are the QFD prediction, the dashed curve is the QED prediction

The combined data of the three experiments yield for the average quark axial vector coupling

$$< g_A^q > \; = \; 0.62 \pm 0.10$$

in good agrement with QFD, where $g_A^q = g_A^{up} = -g_A^{down}$ has been assumed for the up and down type quarks. This is clear evidence that also the light $u$, $d$, $s$ quarks carry the axial vector charges assigned to them in the standard theory.

## 8.3 Total hadronic cross section

The total hadronic cross section normalized to the asymptotic QED cross section for lepton pair production neglecting quark masses can be written as

$$R_{had} \; = \; \sum_q R_{q\bar{q}} \left\{ 1 + \frac{\alpha_s}{\pi} + 1.41 \left(\frac{\alpha_s}{\pi}\right)^2 + 64.8 \left(\frac{\alpha_s}{\pi}\right)^3 + \ldots \right\} . \qquad (49)$$

The sum runs over all quark flavours. The notation is taken from section 3.2 with the electroweak part

$$R_{q\bar{q}} \;=\; 3\left\{Q_q^2 - 2\,g_V^e\,g_V^q\,Q_q\,\Re(\chi) + (g_V^{e\,2}+g_A^{e\,2})(g_V^{q\,2}+g_A^{q\,2})\,|\chi|^2\right\}\,.$$

The factor 3 accounts for the colour and the function $\chi$ contains the $Z^0$ propagator (eqs. (19) or (20)). The terms in curly brackets of eq. (49) represent the QCD corrections due to gluon radiation to third order in the strong coupling constant $\alpha_s$ in the $\overline{MS}$ renormalization scheme assuming 5 quarks.

The bulk of the cross section is given by QED quark pair production, in the naive quark parton model (QPM) $R^{QPM} = 3\sum Q_q^2 = 11/3$ for energies well above the bottom threshold. The QCD corrections decrease with rising energy as a consequence of the running strong coupling constant. The total hadronic cross section offers a clean possibility to measure $\alpha_s$ since the data do not depend on any fragmentation model and the QCD dependence is theoretically calculable. However, recent calculations have shown that the third order corrections are comparable to the second order corrections. The electroweak contributions increase with energy. The QCD and QFD terms have opposite energy behaviours and can thus be separated with very little correlation.

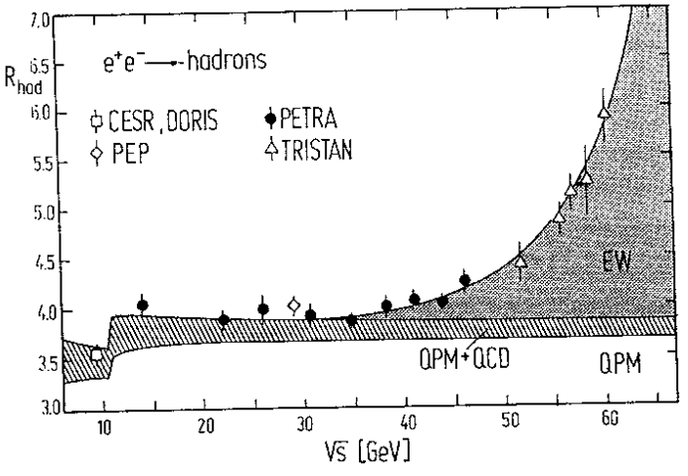


Figure 41: The total hadronic cross section $R_{had}$ as a function of the centre of mass energy. The errors contain statistical and systematic uncertainties and their correlations. The curves represent the fits to the data

The combined total hadronic cross section measurements are shown in Fig. 41 as a function of the centre of mass energy. The rise in $R_{had}$ observed at PETRA between 35 and 46.8 GeV was the first evidence for a direct purely weak $Z^0$ pole contribution,



i.e. not a $\gamma - Z^0$ interference effect, in $e^+e^-$ experiments. This observation is verified by the TRISTAN measurements [84], showing a 50% increase in $R_{had}$ at $\sqrt{s} = 60\,GeV$. The CELLO collaboration [81] and Marshall [82] have performed an analysis using all available cross section data and taking the individual systematic errors and known correlations properly into account. Much care has been given to apply the same higher order radiative corrections to all data. The analysis was recently repeated by [83] including the latest TRISTAN results. A 3 paramter fit to the total hadronic cross section data was performed to determine $\alpha_s$, $\sin^2\theta_W$ and $m_Z$ (assuming a top mass $m_t = 60\,GeV$). The QPM, QCD and electroweak (EW) contributions to the fit are shown in Fig. 41. The strong coupling constant was found to be $\alpha_s(\sqrt{s} = 34\,GeV) = 0.141 \pm 0.019$. The electroweak parameters are

$$\begin{aligned}\sin^2\theta_W &= 0.221\;^{+0.029}_{-0.022}\,,\\ m_Z &= 89.4 \pm 1.9\;GeV\,.\end{aligned}$$

The result on the weak mixing angle $\sin^2\theta_W$, determined at momentum transfers up to $\sim 3500\,GeV^2$, is in very good agreement with the values found in deep inelastic neutrino nucleon scattering and intermediate vector boson production. It is also in remarkable agreement with neutrino electron scattering, polarized electron deuteron scattering and atomic parity violation experiments [5], demonstrating the universality of the weak neutral current coupling over many orders of magnitude in the momentum transfer squared. The mass of the $Z^0$ turns out to be somewhat lower than the values obtained by the $p\bar{p}$ collider experiments at CERN and FNAL. A definite precise answer will be provided soon by the SLC and LEP experiments.

Finally the total cross section data can be used to look for quark substructures, similarly as done for lepton pair production (section 7). Assuming the QFD and QCD terms are given by the previous parameters, any further deviation can be described by a QED like form factor modifying the normalized total hadronic cross section as

$$R'_{had} \;=\; R_{had}\left\{1 \mp \frac{s}{s-\Lambda_\pm^2}\right\}^2\,. \qquad (50)$$

From a fit to the data lower limits (95% confidence level) on the QED cut-off parameters of $\Lambda_+ > 435\,GeV$ and $\Lambda_- > 335\,GeV$ have been obtained [85].

## 8.4 Beyond the standard theory

The electroweak standard theory has been very successful in describing the $e^+e^-$ experiments to a high degree of precision. No new particles or interactions have been found. Limits on the production of new sequential leptons and quarks, supersymmetric particles, neutral and charged Higgs particles have been set with lower limits on the masses close to or beyond the $e^\pm$ beam energy (see refernces in [18]). The known leptons and quarks behave as pointlike particles with no substructure beyond $\sim 10^{-16}\,cm$.

However, it is still conceivable that the electroweak theory is the low energy limit of a more fundamental interaction observable only at very high energy. If 'new

physics' would exist at a mass scale $\Lambda^C$ much larger than the presently accessible momentum transfers $Q$, the interference with the $\gamma$ and $Z^0$ fields would lead to residual contact interactions which may result in deviations from the standard model. A general parametrization of such contact terms, originally intended for substructure or compositeness, has been proposed by [86]. Assuming helicity conservation an effective Lagrangian of the form

$$\mathcal{L}_{eff} = \pm \frac{g^2}{2\,\Lambda_{\pm}^{C\,2}} \{\eta_{LL}\, j_L\, j_L + \eta_{RR}\, j_R\, j_R + 2\,\eta_{LR}\, j_L\, j_R\} \qquad (51)$$

has to be added to the neutral current QFD interaction Lagrangian $\mathcal{L}_I^{NC}$ of section 2. The coupling constant is arbitrarily fixed to $g^2/4\,\pi = 1$, leaving the mass scale $\Lambda^C$ as the only free parameter. $j_L$ and $j_R$ are left-handed and right-handed currents. The coefficients $\eta$ are chosen as 0 or $\pm 1$, allowing to construct left-handed, right-handed, vector and axial vector currents. For the LL coupling $\eta_{LL} = 1$, $\eta_{RR} = \eta_{LR} = 0$, for the RR coupling $\eta_{RR} = 1$, $\eta_{LL} = \eta_{LR} = 0$, for the VV coupling $\eta_{LL} = \eta_{RR} = \eta_{LR} = 1$, and for the AA coupling $\eta_{LL} = \eta_{RR} = -\eta_{LR} = 1$.

A particularly simple example for compositeness is Bhabha scattering. Since initial and final particles are the same no assumptions on the constitutents have to be made. The differential cross section for the reaction $e^+e^- \to e^+e^-$ becomes

$$\begin{aligned}
\frac{d\sigma}{d\Omega} &= \frac{\alpha^2}{8\,s}\left\{4\,B_1 + B_2\,(1-\cos\theta)^2 + B_3\,(1+\cos\theta)^2\right\}\,, \qquad (52)\\
B_1 &= \left(\frac{s}{t}\right)^2 \left|1 + (g_V{}^2 - g_A{}^2)\,\chi(t) \pm \frac{\eta_{LR}\,t}{\alpha\,\Lambda_{\pm}^{C\,2}}\right|^2\,,\\
B_2 &= \left|1 + (g_V{}^2 - g_A{}^2)\,\chi(s) \pm \frac{\eta_{LR}\,s}{\alpha\,\Lambda_{\pm}^{C\,2}}\right|^2\,,\\
B_3 &= \frac{1}{2}\left|1 + \frac{s}{t} + (g_V + g_A)^2\,(\frac{s}{t}\,\chi(t) + \chi(s)) \pm \frac{2\,\eta_{RR}\,s}{\alpha\,\Lambda_{\pm}^{C\,2}}\right|^2\\
&\quad + \frac{1}{2}\left|1 + \frac{s}{t} + (g_V - g_A)^2\,(\frac{s}{t}\,\chi(t) + \chi(s)) \pm \frac{2\,\eta_{LL}\,t}{\alpha\,\Lambda_{\pm}^{C\,2}}\right|^2\,.
\end{aligned}$$

The cross section formula for $s$ channel lepton pair production can be simply obtained by setting all terms proprtional to $s/t$ to zero and dropping the factor 2 in front of $\eta_{RR}$ and $\eta_{LL}$. For quarks the fractional charges have to be considered.

The sensitivity of the Bhabha and $\mu$ pair differential cross sections on various values of the cut-off parameters $\Lambda^C$ are shown in Fig. 42 for TASSO data at $\sqrt{s} = 34.8\ GeV$. The cross sections have been normalized to the QFD prediction. The angular dependences on the chirality structures are markedly different for the two processes.

Typical values of lower limits on the scale parameters $\Lambda^C$ for leptons and quarks are summarized in Table 14. They are of the order of a few TeV depending on the chirality structure. The traditional QED form factor is a special case of the vector type contact interaction, related by $\Lambda^{QED} \simeq \sqrt{\alpha}\,\Lambda^{VV}$. Note that LL and RR interactions cannot be distinguished in leptonic reactions. This is different for quarks,



where up and down type quarks couple differently to left-handed and right-handed currents. Summing over five quarks therefore leads to different LL and RR coupling limits. All quark flavours are assumed to contribute with the same $\Lambda^C$ parameter. However, substructures need not to show up at the same scale for all quark families. If only the $u$ and $d$ quarks are allowed to have a structure while the heavier quarks behave still pointlike the limits are slightly less stringent.

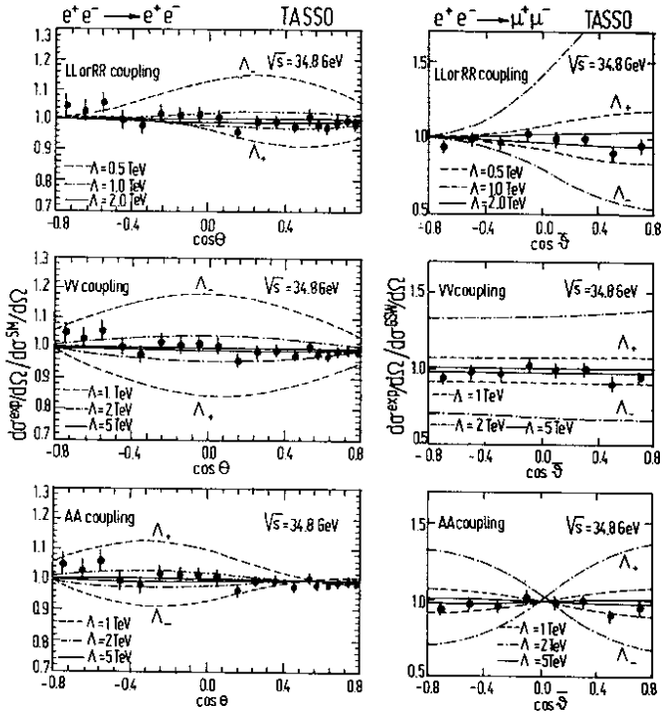


Figure 42: The differential cross sections normalized to QFD for the reations $e^+e^- \to e^+e^-$ and $e^+e^- \to \mu^+\mu^-$ from TASSO at $\sqrt{s} = 34.8\,GeV$. The curves show possible contributions of contact terms for left-handed (LL) or right-handed (RR) coupling, vector (VV) coupling, and axial vector (AA) coupling

Table 14: Lower limits (95% confidence level) of mass scale parameters $\Lambda^C\,[TeV]$ in contact interactions for left-handed (LL), right-handed (RR), vector (VV), and axial vector (AA) couplings

| Reaction | $\Lambda_+^{LL}$ | $\Lambda_-^{LL}$ | $\Lambda_+^{RR}$ | $\Lambda_-^{RR}$ | $\Lambda_+^{VV}$ | $\Lambda_-^{VV}$ | $\Lambda_+^{AA}$ | $\Lambda_-^{AA}$ |
|---|---|---|---|---|---|---|---|---|
| $e^+e^- \to e^+e^-$ [38] | 1.4 | 3.3 | 1.4 | 3.3 | 3.6 | 7.1 | 2.8 | 2.4 |
| $e^+e^- \to \mu^+\mu^-$ [47] | 2.3 | 1.3 | 2.3 | 1.3 | 3.5 | 1.8 | 3.2 | 2.9 |
| $e^+e^- \to \tau^+\tau^-$ [49] | 2.2 | 3.2 | 2.2 | 3.2 | 2.7 | 5.7 | 4.1 | 5.7 |
| $e^+e^- \to q\bar{q}$ [85] | 1.2 | 1.8 | 3.4 | 2.7 | 5.1 | 3.9 | 1.7 | 2.4 |

# 9. Conclusion

The impressive amount of data accumulated by high energy electron-positron collision experiments at PETRA, PEP and TRISTAN during the past decade allows to test the fundamental interactions very precisely. Tests of Quantum Electrodynamics, the paradigm of all field theories, at unprecedented high time-like momentum transfers of up to $s \sim 3000\,GeV^2$ confirm its validity to $\mathcal{O}(\alpha^3)$ and $\mathcal{O}(\alpha^4)$ within a few percent, but also clearly unvealed the presence of electroweak effects in lepton and hadron final states. The quality of the QED tests gives confidence in extracting the electroweak parameters of the standard theory. The embracing theory Quantum Flavourdynamics provides a coherent description of all observations at the ten percent level. The $e^+e^-$ experiments contribute in particular information on the heavy lepton and quark families which cannot be obtained in other experiments.

The main achievements of electron-positron collisions with respect to QED and QFD tests are:

- The reaction $e^+e^- \to \gamma\gamma$, the only process where QED can be tested as a self consistent theory, has been measured very precisely and confirms QED including radiative corrections to $\mathcal{O}(\alpha^3)$ at the one percent level. QED cut-off parameters exceeding $\Lambda > 80\,GeV$ have been derived.

- The total cross sections for lepton pair production $e^+e^- \to e^+e^-$, $e^+e^- \to \mu^+\mu^-$ and $e^+e^- \to \tau^+\tau^-$ have been measured at the level of a few percent and agree with $\mathcal{O}(\alpha^3)$ QED calculations. QED cut-off parameters larger than $\Lambda > 250\,GeV$ have been obtained, indicating that all three leptons behave as pointlike particles down to a distance of about $10^{-16}\,cm$.

- Hard photon radiation with one and two additional photons accompanying the basic two particle final states has been studied and verifies the $\mathcal{O}(\alpha^3)$ and $\mathcal{O}(\alpha^4)$ QED calculations to better than 10%. It has to be stressed that large efforts have been devoted to the development of Monte Carlo event generators including the higher order virtual and bremsstrahlung radiative corrections, which are able to reproduce the experimental results reliably.



- Photon-photon collisons $e^+e^- \to e^+e^-e^+e^-$ and $e^+e^- \to e^+e^-\mu^+\mu^-$ have been investigated and show that the total cross section for untagged $e^+e^- \to e^+e^-\mu^+\mu^-$ events becomes larger than the annihilation cross section for $e^+e^- \to \mu^+\mu^-$ at high energy. Although the momentum transfers are moderate compared to the annihilation processes photon-photon collisions demonstrate the nice agreement with $\mathcal{O}(\alpha^4)$ QED calculations.

- Electroweak $\gamma - Z^0$ interference effects have been observed in lepton and quark production. Sizeable forward backward charge asymmetries have been established for the reactions $e^+e^- \to \mu^+\mu^-$ and $e^+e^- \to \tau^+\tau^-$. The electroweak parameters of the three charged leptons agree with each other and with the standard theory and support the concept of $e - \mu - \tau$ lepton universality. The axial vector charges of the heavy quarks as well as of the light quarks have been investigated and found to be in good agreement with the QFD assignments.

- The definite rise of the normalized total hadronic cross section at centre of mass energies above 35 GeV is the first evidence for direct contributions from the $Z^0$ resonance in $e^+e^-$ collisions. The electroweak mixing angle derived from these measurements is comparable and competitive to the values found in other experiments.

The next generation of $e^+e^-$ experiments at SLC and LEP just start their physics program at energies around the $Z^0$ resonance. They aim at precision tests of the electroweak theory, which rely sensitively on the understanding of higher order electroweak radiative corrections. QED can therefore only be seen in the context of QFD and QCD. The only area which will remain a domain of QED for quite some time will be photon pair production $e^+e^- \to \gamma\gamma$ and lepton pair production by photon-photon collisions $e^+e^- \to e^+e^-l^+l^-$.

**Acknowledgements.** I would like to thank my colleagues from the TASSO collaboration and from the other experiments at PETRA and PEP for the numerous dicussions which helped in understanding the physics of electron-positron collisions. My special thanks go to D. Haidt for critical reading of the manuscript.

## References


[1] D. Haidt and H. Pietschmann. *Electroweak Interactions.* Volume I/10 of *Landolt - Börnstein, New Series*, Springer Verlag, Berlin Heidelberg, 1988.

[2] S.L. Glashow. *Nucl. Phys.* **22** (1961) 579 and *Rev. Mod. Phys.* **52** (1980) 539.

[3] A. Salam. *Phys. Rev.* **127** (1962) 331 and *Rev. Mod. Phys.* **52** (1980) 525.

[4] S. Weinberg. *Phys. Rev. Lett.* **19** (1967) 1264 and *Rev. Mod. Phys.* **52** (1980) 515.

[5] P. Langacker. Proc. xxiv Int. Conf. on High Energy Physics, Munich (1988), 190.

[6] F. M. Renard. *Basics of Electron Positron Collisions.* Edition Frontières, Gif sur Yvette, France, 1981.

[7] S.L. Glashow, J. Iliopoulos, and L. Maiani. *Phys. Rev.* **D2** (1970) 1285.

[8] Particle Data Group. *Phys. Lett.* **204B** (1988) 1.

[9] R. Budny. *Phys. Lett.* **55B** (1975) 227.

[10] F.A. Berends and A. Böhm. Lepton pair production, radiative corrections and electroweak parameters. In A. Ali and P. Söding, editors, *High Energy Electron–Positron Physics*, World Scientific Publishing, Signapore, 1988.

[11] M. Böhm and W. Hollik. *Phys. Lett.* **139B** (1984) 213.

[12] F.A. Berends and R. Kleiss. *Nucl. Phys.* **B186** (1981) 22.

[13] F.A. Berends, R. Kleiss, and S. Jadach. *Nucl. Phys.* **B202** (1982) 63.

[14] S. Jadach and Z. Was. *Acta Phys. Pol.* **B15** (1984) 1151.

[15] F.A. Berends and R. Kleiss. *Nucl. Phys.* **B228** (1983) 537.

[16] F.A. Berends, P.H. Daverveldt, and R. Kleiss. *Comp. Phys. Comm.* **40** (1986) 271, 285, 309.

[17] V.M. Budnev, I.F. Ginzburg, G.V. Meledin, and V.G. Serbo. *Phys. Rep.* **15** (1975) 181.

[18] A. Ali and P. Söding, editors. *High Energy Electron–Positron Physics.* Volume 1 of *Advanced Series on Directions in High Energy Physics*, World Scientific Publishing, Signapore, 1988.

[19] S.D. Drell. *Ann. Phys.* **41** (1958) 75.

[20] A. Litke. Ph.D. Thesis, Harvard University, unpublished (1970).

[21] HRS Coll., M. Derrick *et al. Phys. Lett.* **166B** (1986) 468.

[22] HRS Coll., M. Derrick *et al. Phys. Rev.* **D34** (1986) 3286.





[23] MAC Coll., E. Fernandez *et al. Phys. Rev.* **D35** (1987) 1.

[24] CELLO Coll., H.J. Behrend *et al. Phys. Lett.* **168B** (1986) 420.

[25] JADE Coll., W. Bartel *et al. Z. Phys.* **C19** (1983) 197.

[26] MARK J Coll., B. Adeva *et al. Phys. Rev. Lett.* **53** (1984) 134.

[27] PLUTO Coll., C. Berger *et al. Phys. Lett.* **94B** (1980) 87.

[28] TASSO Coll., M. Althoff *et al. Z. Phys.* **C26** (1984) 337.

[29] AMY Coll., S.K. Kim *et al. Phys. Lett.* **223B** (1989) 476.

[30] TOPAZ Coll., I. Adachi *et al. Phys. Lett.* **200B** (1988) 391.

[31] VENUS Coll., K. Abe *et al.* subm. to *Z. Phys.* **C** (1989).

[32] HRS Coll., M. Derrick *et al. Phys. Lett.* **166B** (1986) 463.

[33] MAC Coll., E. Fernandez *et al. Phys. Rev.* **D35** (1987) 10.

[34] CELLO Coll., H.J. Behrend *et al. Phys. Lett.* **103B** (1981) 148.

[35] JADE Coll., W. Bartel *et al. Z. Phys.* **C30** (1986) 371.

[36] MARK J Coll., B. Adeva *et al. Phys. Rep.* **109** (1984) 133.

[37] PLUTO Coll., C. Berger *et al. Z. Phys.* **C27** (1985) 341.

[38] TASSO Coll., W. Braunschweig *et al. Z. Phys.* **C37** (1988) 171.

[39] Y. Unno. Proc. xxiv Int. Conf. on High Energy Physics, Munich (1988), 860.

[40] HRS Coll., M. Derrick *et al. Phys. Rev.* **D31** (1985) 2352.

[41] HRS Coll., K.K. Gan *et al. Phys. Lett.* **153B** (1985) 116.

[42] MAC Coll., D. Bender *et al. Phys. Rev.* **D30** (1985) 515.

[43] CELLO Coll., H.J. Behrend *et al. Phys. Lett.* **183B** (1987) 400.

[44] CELLO Coll., H.J. Behrend *et al. Phys. Lett.* **114B** (1982) 282.

[45] MARK J Coll., B. Adeva *et al. Phys. Lett.* **179B** (1986) 177.

[46] PLUTO Coll., L. Criegee and G. Knies. *Phys. Rep.* **83** (1982) 153.

[47] TASSO Coll., W. Braunschweig *et al. Z. Phys.* **C40** (1988) 163.

[48] TASSO Coll., W. Braunschweig *et al.* DESY 89-035, subm. to *Z. Phys.* C.

[49] B. Naroska. *Phys. Rep.* **148** (1986) 67.

[50] CELLO Coll., H.J. Behrend *et al. Phys. Lett.* **158B** (1985) 536.

[51] MAC Coll., W.T. Ford *et al. Phys. Rev. Lett.* **51** (1983) 257.

[52] MARK J Coll., B. Adeva *et al. Phys. Rev.* **D38** (1988) 2665.

[53] MARK J Coll., B. Adeva *et al. Phys. Rev. Lett.* **55** (1985) 665.

[54] MAC Coll., E. Fernandez *et al. Phys. Rev.* **D28** (1983) 2721.

[55] PEP-9 $\gamma\gamma$ Coll., M.P. Cain *et al. Phys. Lett.* **147B** (1984) 232.

[56] CELLO Coll., H.J. Behrend *et al. Z. Phys.* **C43** (1989) 1.

[57] JADE Coll., W. Bartel *et al. Z. Phys.* **C30** (1986) 545.

[58] PLUTO Coll., C. Berger *et al. Z. Phys.* **C27** (1985) 249.

[59] Ch. Berger and W. Wagner. *Phys. Rep.* **146** (1987) 1.

[60] JADE Coll., W. Bartel *et al. Phys. Lett.* **161B** (1985) 188.

[61] PLUTO Coll., C. Berger *et al. Z. Phys.* **C28** (1985) 1.

[62] J.G. Branson. Proc. Int. Symp. on Lepton and Photon Interactions, Bonn (1981), 279.

[63] MAC Coll., W.W. Ash *et al. Phys. Rev. Lett.* **55** (1985) 1831.

[64] MARK II Coll., M.E. Levi *et al. Phys. Rev. Lett.* **51** (1983) 1941.

[65] CELLO Coll., H.J. Behrend *et al. Phys. Lett.* **191B** (1987) 209.

[66] PLUTO Coll., C. Berger *et al. Z. Phys.* **C21** (1983) 53.

[67] S.L. Olsen. Proc. xxiv Int. Conf. on High Energy Physics, Munich (1988), 868.

[68] MAC Coll., E. Fernandez *et al. Phys. Rev. Lett.* **54** (1985) 1620.

[69] ARGUS Coll., H. Albrecht *et al. Phys. Lett.* **192B** (1987) 245.

[70] HRS Coll., P. Baringer *et al. Phys. Lett.* **206B** (1988) 551.

[71] TPC Coll., H. Aihara *et al. Phys. Rev.* **D34** (1986) 1945.

[72] JADE Coll., F. Ould-Saada *et al.* DESY 89-063, subm. to *Z. Phys.* C.

[73] TASSO Coll., W. Braunschweig *et al.* DESY 89-053, subm. to *Z. Phys.* C.

[74] N.S. Lockyer. SLAC-PUB 3245 (1983).

[75] C. Kiesling. Proc. xxiv ème Rencontre de Moriond (1989).

[76] JADE Coll., W. Bartel *et al. Phys. Lett.* **146B** (1984) 437.

[77] P. Rehders. Ph.D. Thesis, Hamburg University, unpublished (1989).

[78] MAC Coll., W.W. Ash *et al. Phys. Rev. Lett.* **58** (1987) 1080.



[79] TASSO Coll., W. Braunschweig *et al. Z. Phys.* **C41** (1988) 385.

[80] JADE Coll., T. Greenshaw *et al. Z. Phys.* **C42** (1989) 1.

[81] CELLO Coll., H.J. Behrend *et al. Phys. Lett.* **183B** (1987) 400.

[82] R. Marshall. *Z. Phys.* **C43** (1989) 607.

[83] G. D'Agostini, W. de Boer, and G. Grindhammer. DESY 89-057.

[84] T. Kamae. Proc. xxiv Int. Conf. on High Energy Physics, Munich (1988), 156.

[85] H.-U. Martyn. Proc. of the HERA workshop, Hamburg, (1987) Vol. 2, 811.

[86] E.J. Eichten, K.D. Lane, and M.E. Peskin. *Phys. Rev. Lett.* **50** (1983) 811.

# List of Tables





# List of Figures